Measurement Report: Characterization of Aerosol Hygroscopicity over Southeast Asia during the NASA CAMP²Ex Campaign

Genevieve Rose Lorenzo[1,2], Luke D. Ziemba[3], Avelino F. Arellano[1], Mary C. Barth[4], Ewan C. Crosbie[3,5], Joshua P. DiGangi[3], Glenn S. Diskin[3], Richard Ferrare[3], Miguel Ricardo A. Hilario[1], Michael A. Shook[3], Simone Tilmes[4], Jian Wang[6], Qian Xiao[6], Jun Zhang[4], and Armin Sorooshian[1,7]

[1]Department of Hydrology and Atmospheric Sciences, University of Arizona, Tucson, Arizona, 85721, USA
[2]Manila Observatory, Quezon City, 1108, Philippines
[3]NASA Langley Research Center, Hampton, Virginia, 23681 USA
[4]Atmospheric Chemistry Observations & Modeling Laboratory, NSF National Center for Atmospheric Research, Boulder, Colorado, 80301, USA
[5]Analytical Mechanics Associates, Inc, Hampton, Virginia, 23666 USA
[6]Department of Energy, Environmental & Chemical Engineering, Washington University in St Louis, St. Louis, Missouri, 63130, USA
[7]Department of Chemical and Environmental Engineering, University of Arizona, Tucson, Arizona, 85721, USA

Correspondence to: armin@arizona.edu

Abstract. This study characterizes the spatial and vertical nature of aerosol hygroscopicity in Southeast Asia and relates it to aerosol composition and sources. Aerosol hygroscopicity via the light scattering hygroscopic growth factor, $f(RH)$, is calculated from the amplification of PM_5 aerosol ($D_p < 5$ μm) scattering measurements from $< 40\%$ % to 82% % relative humidity during the Cloud, Aerosol, and Monsoon Processes Philippines Experiment (CAMP²Ex) between August to October 2019 over the northwest tropical Pacific. Median $f(RH)$ is low (1.26 with lower to upper quartiles of 1.05 to 1.43) like polluted environments, due to the dominance of the mixture of organic carbon and elemental carbon. The $f(RH)$ is lowest due to smoke from the Maritime Continent (MC) during its peak biomass burning season, coincident with high carbon monoxide concentrations (> 0.25 ppm) and pronounced levels of accumulation mode particles and organic mass fractions. The highest $f(RH)$ values are linked to coarser particles from the West Pacific and aged biomass burning particles in the region farthest away from the MC, where $f(RH)$ values are lower than typical polluted marine environments. Convective transport and associated cloud processing in these regions decrease and increase hygroscopicity aloft in cases with transported air masses exhibiting increased organic and sulfate mass fractions, respectively. An evaluation of a global chemical transport model (CAM-chem) for cases of vertical transport showed the underrepresentation of organics resulting in overestimated modeled aerosol hygroscopicity. These findings on aerosol hygroscopicity can help to improve aerosol representation in models and the understanding of cloud formation.

1. Introduction

Aerosol particles affect climate and visibility through the direct and indirect extinction of solar radiation via absorption and scattering of light and through cloud formation, respectively. Aerosol hygroscopicity compounds aerosol effects on Earth's radiation budget (Zhao et al., 2018; Malm and Day, 2001), secondary aerosol formation and cloud formation (Köhler, 1936), and health (Dockery, 2001). Neglecting the effect of moisture on aerosol growth leads to incorrect estimation of the cooling at Earth's surface due to aerosol particles (Garland et al., 2007). For instance, a decrease in light extinction over the southeast U.S. was linked to reduced aerosol water uptake, coincident with decreases in the sulfate/organic ratio (Attwood et al., 2014). Particle aging/coating can cause underestimation of both aerosol hygroscopicity in the sub-saturated regime (Wang et al., 2018) and cloud condensation nuclei (CCN) activity in the supersaturated regime for aged particles in China by ~22% (Zhang et al., 2017). Remote sensing of aerosol optical properties is also affected by aerosol water content (Ferrare et al., 1998; Ferrare et al., 2023). Therefore, accurate aerosol hygroscopicity values are critical for remote sensing and satellite observation of aerosol particles (Ziemba et al., 2013; Van Diedenhoven et al., 2022).

Aerosol hygroscopicity is described by physical quantities such as the diameter growth factor, g(RH), and light scattering hygroscopic growth factor, f(RH). The g(RH) parameter relates the wet particle diameter of the aerosol at a high relative humidity to the dry diameter of the aerosol at low relative humidity, while f(RH) relates total scattering due to the aerosol at high relative humidity (80%) to that at low relative humidity (<40%) (Waggoner et al., 1983; Hegg et al., 1993). Light scattering increases with relative humidity for most particles and is correlated to chemical composition and size (Baynard et al., 2006; Swietlicki et al., 2008) of particulate matter (Covert et al., 1972; Brock et al., 2016a).

Direct measurement of aerosol hygroscopicity, however, is difficult and is also not well-represented in climate models (Chen et al., 2014). The hygroscopicity parameter kappa, κ, is a single parameter that was developed to represent water uptake in models. It determines the volume (or mass or moles, with appropriate unit conversions) of water that is associated with a unit volume of a dry aerosol particle (Petters and Kreidenweis, 2007). A simple and commonly used water uptake model for calculating kappa is based on the Zdanovskii, Stokes, and Robinson (ZSR) treatment for water soluble organic-inorganic mixed aerosol particles (Stokes and Robinson, 1966) where it is assumed that there are no interactions between the organic and inorganic species. In the ZSR model, water uptake of the individual non-interacting components can be summed up linearly to represent the total water uptake of the mixed aerosol. The interaction of organics and inorganics, however, along with the aging-specific density of organics is thought to influence hygroscopicity and affect both the ZSR calculation (Fan et al., 2020) and aerosol particle growth factor via changes in molecular structure, molecular weight, functionality, and/or other properties (Swietlicki et al., 2008).

Table 1: Hygroscopicity values of various aerosol types based on selected summary studies for measured g(RH) (Swietlicki et al., 2008) and f(RH) (Burgos et al., 2019; Titos et al., 2021) and modeled κ (Pringle et al., 2010).

68 Observed and simulated aerosol hygroscopicity using aforementioned parameters are greater (Table 1) in clean marine

69 air masses (f(RH=85 %/RH=40 %) = 2.10 - 2.30 for PM$_1$) compared to air masses over land, and near terrestrial

70 biogenic sources (f(RH=85 %/RH=40 %) = 1.29 - 2.10 for PM$_1$), which are secondary organics precursors, and under

71 polluted conditions from biomass burning (f(RH=85 %/RH=40 %) = 1.02 – 2.10 for PM$_1$) (Swietlicki et al., 2008;

72 Duplissy et al., 2011; Petters and Kreidenweis, 2007; Burgos et al., 2019; Titos et al., 2021; Gomez et al., 2018). Only

73 the Arctic has aerosol hygroscopicity (f(RH=85 %/RH=40 %) = 2.70 for PM$_1$ and f(RH=85 %/RH=40 %) = 3.00 for

74 whole-air samples) values greater than in clean marine regions (Delene and Ogren, 2002; Zieger et al., 2010). In

75 marine areas, hygroscopicity typically decreases with altitude with decreasing inorganic fractions (Pringle et al.,

76 2010). Cloud processing over marine areas has been observed to increase the oxidation of organic aerosols (Che et al.,

77 2022; Dadashazar et al., 2022) and hygroscopicity in general (Crumeyrolle et al., 2008). Continental aerosol particles

78 have smaller diameters and are usually less hygroscopic due to more organic-rich aerosol particles (κ = 0 - 0.1 from

79 Table S1) and pure elemental carbon particles (EC, κ = 0 - 0.035 from Table S1) (Wang et al., 2014; Kreidenweis and

80 Asa-Awuku, 2014). Organics are generally less hygroscopic than inorganics (κ = 0.56 – 1.24 from Table S1), and

81 their hygroscopicity is affected by oxidation level (e.g., O:C ratio), oxidation state, and solubility (Brock et al., 2016a;

82 Wu et al., 2016; Thalman et al., 2017). Aging has also been found to increase aerosol hygroscopicity through the

83 oxidation of secondary organic aerosols and organic aerosol interactions with inorganics (Engelhart et al., 2008; Liu

84 et al., 2014; Saxena et al., 1995).

85 Although aerosol studies in the rapidly developing Southeast Asia (SEA) region are increasing, few are focused on

86 the nature of aerosol particles and their interactions with water vapor and clouds (Tsay et al., 2013; Ross et al., 2018;

87 Reid et al., 2023). There has been no comprehensive study of aerosol hygroscopicity in and around the Philippines in

88 Southeast Asia. Understanding the interactions between aerosols and the complex geographic, meteorological, and

89 hydrological environment in Southeast Asia remains challenging due to a still growing observational database,

90 prevalence of clouds interfering with remote sensing, and limited modeling studies (Tsay et al., 2013; Lee et al., 2018;

91 Chen et al., 2020; Hong and Di Girolamo, 2020; Amnuaylojaroen, 2023). This, along with increased local and

92 transported emissions and prevalent moisture-rich conditions in the region, altogether motivate the need to understand

93 aerosol hygroscopicity and associated impacts on radiative transfer and on climate (Brock et al., 2016a; Ziemba et al.,

94 2013). How freshly emitted nearly hydrophobic particles transform into hygroscopic aerosol particles (Swietlicki et

95 al., 2008), for example, is an understudied topic in Southeast Asia where there are significant sources of particles

96 with low hygroscopicity (Reid et al., 2023). Understanding aerosol hygroscopicity will also help in the need to improve

97 remote sensing measurements in the region, which is affected by overlapping high and low level clouds (Burgos et

98 al., 2019; Hong and Di Girolamo, 2020).

99 Predicting aerosol hygroscopicity, especially at higher relative humidity (RH), is especially difficult due to optical

100 instruments underestimating particle light scattering at high RH and mechanisms other than hygroscopicity impacting

101 particle growth (Gasparini et al., 2006; Mochida et al., 2006). This is important because atmospheric water content is

102 high in Southeast Asia. For example, the hygroscopicity of secondarily formed organics (via gas-to-particle

103 conversion) is found to be dependent on oxidation state for high RH (Shi et al., 2022). Southeast Asia has elevated

104 levels of organics, inorganics, and elemental carbon (Cruz et al., 2019; Azadiaghdam et al., 2019; Oanh et al., 2006),

105 allowing for an opportunity to see how hygroscopicity responds to a range of relative values of each of these elevated

106 components. Therefore, relating aerosol particle composition to hygroscopicity, for closure (Xu et al., 2020), is

107 particularly significant there.

108 Aerosol hygroscopicity is a crucial factor in the understanding and modeling of aerosol-cloud interactions, because of

109 the role hygroscopicity plays in cloud drop activation. The NASA Cloud, Aerosol, and Monsoon Processes Philippines

110 Experiment (CAMP^{2}Ex) was designed to understand the role of aerosol particles in cloud formation and in regulating

111 solar radiation during the southwest monsoon (Reid et al., 2023). CAMP^{2}Ex occurred between August and October

112 2019 over the Philippines and neighboring areas. The campaign provides an aircraft dataset with measurements

113 focused on aerosol and cloud properties, which affords a valuable opportunity to evaluate models with these

114 measurements for shallow to moderate convection, which is one of the biggest challenges for regional and global-

115 scale atmosphere models to represent because these clouds are much smaller than the model grid spacing.

116 Global atmospheric model evaluation of aerosol extinction for the CAMP^{2}Ex region suggests that biomass burning

117 aerosol hygroscopicity is over-estimated by global atmosphere models, with both the model size representation of the

118 aerosol particles and the size discrepancy between model and observations contributing to this (Collow et al., 2022;

119 Edwards et al., 2022). The findings from Collow et al. (2022) and Edwards et al. (2022) bring up the need for a more

120 thorough understanding of the components of biomass burning aerosols in the region that affect observed and modeled

121 hygroscopicity. The overestimation of hygroscopicity due to biomass burning can affect the representation of clouds

122 in the region. Clouds, especially shallow cumulus clouds, like those in the tropical West Pacific (which the CAMP^{2}Ex

123 region is part of) have been underestimated by models due to the lack of observational data to improve convective

124 parameterizations (Chandra et al., 2015). Part of the challenge in modeling aerosol-cloud interactions is the ability to

125 both have a high-resolution representation, at the scale of the shallow convection, in a large enough domain, which is

126   important for understanding climatic effects to properly account for the bulk behavior of cloud fields (Spill et al.,
127   2019). This could be addressed by evolving modeling infrastructures, with higher resolution schemes ranging from
128   regional to convective scale within a larger domain (Pfister et al., 2020; Radtke et al., 2021).

129   Knowledge gaps identified above are addressed in this study using the CAMP^{2}Ex dataset. To our knowledge, this is
130   the first time this dataset has been explored extensively to characterize aerosol hygroscopicity properties in the region.
131   The goals of this proposed study are to (i) characterize the spatial distribution of aerosol hygroscopicity in Southeast
132   Asia during the CAMP^{2}Ex airborne mission, (ii) relate aerosol hygroscopicity and composition, (iii) identify emission
133   events that impact aerosol hygroscopic growth, and (iv) evaluate a global chemical transport model with regional
134   refinement for aerosol vertical transport.

135

136   **2. Methods**

137   **2.1 CAMP^{2}Ex Field Campaign**

138   CAMP^{2}Ex included 19 research flights with a NASA P3 from 24 August to 5 October 2019. Twelve of these flights
139   were associated with the southwest monsoon (SWM) followed by a flow reversal with seven flights conducted during
140   the northeast monsoon (NEM) (Reid et al., 2023). As summarized by Reid et al. (2023), the combination of airborne
141   and ship-based measurements helps to characterize interactions between various aerosol particle sources (e.g., biomass
142   burning, industrial, natural) and small to congestus convection. Below we note the P3 instruments most relevant to
143   this study.

144   **2.2 Observations and Derived Quantities**

145   **2.2.1 P3 Instrumentation**

146   As summarized in Table 2̶1, data are used from a variety of aerosol particle and trace gas instrumentation. The aerosol
147   particle scattering and absorption instruments measure the optical properties of bulk aerosol particles (PM$_5$): < 5 μm
148   dry diameter (Mcnaughton et al., 2007). Aerosol composition and size data for submicrometer particles were
149   considered when they were collected using a forward-facing shrouded isokinetic inlet. Non-refractory species in the
150   submicrometer range studied using an aerosol mass spectrometer (AMS) included sulfate, nitrate, ammonium,
151   organics, and chloride. We also use the ratio of the mass spectral marker m/z 44 marker relative to total organic mass,
152   f$_{44}$, as a possible indicator of air mass age. Submicrometer refractory species of black carbon (also referred to as
153   elemental carbon) from a single particle poot photometer (SP2) were also included in the study. Bulk water-soluble
154   aerosol particles were collected using a particle-into-liquid sampler (PILS) and were analyzed using ion
155   chromatography; species quantified included oxalate, NH_4^+, dimethylamine (DMA), K^+, SO_4^{2-}, Ca^{2+}, Na^+, Mg^{2+}, Cl^-,
156   NO_3^-, Br^-, and NO^-. Cloud-free conditions are identified to ensure the highest quality aerosol data using a cloud flag
157   product based on measurements from the fast cloud droplet probe (FCDP) and two-dimensional stereo probe (2D-S).
158   Aerosol particle composition data are considered for those cases when the total aerosol non-refractory particle mass
159   was greater than 0.4 μg sm^{-3}.

160   **Table 21: Summary of instrument data used in this work.**

Parameter	Instrument	Time Resolution	Uncertainty	Sampled Aerosol Particle Size	Reference
Latitude, Longitude, and Altitude	Northrop Grumman Litton 251 EGI	1 s	~5 m spherical error probable; 0.01°	N/A	Reid et al., 2023
Dry (RH < 40 %) and humidified (RH = 80 %) light scattering coefficient (λ = 450, 550, 700 nm)	Parallel humidified TSI 3563 Nephelometers	1 s	30 %	< 5 μm diameter	Ziemba et al., 2013; McNaughton et al., 2007
Dry (RH < 40 %) light absorption coefficient (λ = 470, 532, 660 nm)	Radiance Research 3 Particle Soot Absorption Photometer (PSAP)	1 s	15 %	< 5 μm diameter	Mason et al., 2018; McNaughton et al., 2007
Non-refractory aerosol (Organics, SO_4, NO_3, NH_4, Cl) mass concentration	Aerodyne High-Resolution Time-of-Flight Mass Spectrometer (AMS)	25 s	LLOD (μg sm^{-3}): Organics, 0.169; SO_4, 0.039; NO_3, 0.035; NH_4, 0.169; Cl, 0.036; Uncertainty: 50 %	approximate relevant size range is 60-600 nm vac. aero. diameter	DeCarlo et al., 2008
Water-soluble mass concentration	Particle-into-liquid sampler (PILS) followed by offline ion chromatography analysis	238 s	30 %	< 5μm diameter	Sorooshian et al., 2006 Crosbie et al., 2020
Refractory black carbon (BC) mass concentration	Single Particle Soot Photometer (DMT SP2)	1 s	10 %	100 - 700 nm diameter	Schwarz et al., 2006
CO concentration	Picarro G2401-m	1 s	5 ppb	N/A	DiGangi et al., 2021
Volume and number concentration of particles	TSI Laser Aerosol Spectrometer (LAS) Model 3340	1 s	20 %	0.1 - 5 μm optical diameter	Moore et al., 2021
Volume size distribution	Fast integrated mobility spectrometer (FIMS)	1 s	Concentration: 15 %; Size: 3 %	10 – 500 nm mobility diameter	Kulkarni and Wang, 2006;

					Wang et al., 2017; 2018
Cloud particles (data used for cloud screening)	SPEC-Hawkeye FCDP	1 s	50~~%~~ %	2 – 50 μm diameter	Knollenberg 1981, Lawson et al. 2017; Woods et al. 2018
Cloud particles (data used for cloud screening)	SPEC-Hawkeye 2D-S	1 s	20~~%~~ %	10 μm – 3 mm diameter	Lawson et al. 2006a, Woods et al. 2018

161

162 **2.2.2 Aerosol Hygroscopicity, *f*(RH), and Other Aerosol Optical Properties**

163 Aerosol hygroscopicity is reported using the parameter *f*(RH), which is unitless and is the amplification factor in

164 scattering due to a change in RH. The *f*(RH) parameter is calculated from the empirically derived exponential fit

165 coefficient gamma (γ) (Ziemba et al., 2013). The gamma parameter is based on parallel nephelometer measurements

166 of scattering at 550 nm at two different relative humidity levels: dry (< 40~~%~~ %: RH_{dry}) and humidified (controlled to

167 82 ± 10~~%~~ %: RH_{wet}). ~~ ~~Gamma (Eq. 1) was calculated for times when the dry (SC_{dry}) and humidified (SC_{wet}) scattering

168 coefficients (Table ~~2~~1) are greater than or equal to 5 Mm^{-1}. The *f*(RH) (Eq. 2) was then derived from γ (Hänel, 1976).

169

170
$$\gamma = \frac{\ln\frac{SC_{wet}}{SC_{dry}}}{\ln\frac{100 - RH_{dry}}{100 - RH_{wet}}} \quad \quad (1)$$

171
$$f(RH) = (\frac{100 - RH_{wet}}{100 - RH_{dry}})^{-\gamma} \quad \quad (2)$$

172 Each nephelometer was calibrated with pure CO_2 prior to the campaign and zero checks were performed periodically

173 during the flights to prevent baseline drift. ~~Hydrophilic polystyrene latex (PSL) aerosol were also introduced~~

174 ~~periodically in flight to ensure the nephelometers were consistent.~~ All nephelometer scattering coefficient

175 measurements were corrected for truncation errors using a documented method (Anderson and Ogren, 1998). System

176 response was verified in flight by introducing hydrophobic PSL spheres into the sample stream to ensure that the

177 nephelometers were consistent and an *f*(RH) value of 1.0 is observed. Relative humidity measurements for the

178 calculation of *f*(RH) were calibrated in the laboratory using nebulized monodisperse 200 nm ammonium sulfate to

179 ensure deliquescence at ~80~~%~~ % RH and at the typical measurement flow rates (i.e. 10 L min^{-1}) (Brooks et al., 2002).

180 The RH was slowly ramped up from ~60~~%~~ % – 90~~%~~ % and the apparent deliquescence RH was calculated based on

181 the sharp increase in scattering in the humidogram. The offset between the calculated RH and the deliquescence RH

182 for ammonium sulfate (i.e., ~79.5~~%~~ %) was applied to the data post-processing. Calibration at ~80~~%~~ % RH increases

183 the confidence in the humidified nephelometer data accuracy. Non-linearities can occur at low RH measurements and

184 add to uncertainties, but the *f*(RH) calculation is much less sensitive at the dry end of the spectrum. Internal RH sensors

185   were used because their placement is most relevant to the sampling condition inside the nephelometer. Note that

186   sampling efficiency decreases for supermicrometer diameter particles with increasing size up to the 5-µm inlet cutoff,

187   due to losses in transport tubing and in the drying/humidification control system. Thus, derived f(RH) is applicable to

188   accumulation-mode particles and is partially sensitive to coarse-mode particles from 1-5 µm diameter.

189

190   Single scattering albedo (SSA) was calculated when both the scattering and absorption coefficients (smoothed with

191   30 s running average) were greater than 2 Mm^{-1}. The Ångström exponent (AE) was calculated using the smoothed 30

192   s running average of the scattering and absorption coefficients. The scattering Ångström exponent (SAE, 450-700

193   nm) was computed when the scattering coefficient was greater than 2 Mm^{-1} based on Ziemba et al. (2013) and the

194   absorption Ångström exponent (AAE, 470-660 nm) was computed when the absorption coefficient was greater than

195   2 Mm^{-1} to try to minimize noise issues (Mason et al., 2018). Absorption measurements were corrected for a variety of

196   errors using the method from Virkkula (Virkkula, 2010). The PSAP filters were changed before transmission dropped

197   below 70% %. This standard practice minimizes non-linearity effects due to filter loading.

198

199   **2.2.3 Sea Salt**

200   Bulk sea salt mass concentration was calculated using summed PILS concentrations of Na$^+$, Cl$^-$, and Mg^{2+} along with

201   the respective concentrations of the mass concentrations of K$^+$, Ca^{2+} and SO$_4^{2-}$ in sea salt (0.037, 0.04 and 0.25,

202   respectively, by mass) (Crosbie et al., 2022).

203

204   **2.2.4 Aerosol Particle Classification**

205   Aerosol particle optical data were grouped depending on their AAE and SAE (Section 2.2.2) values and based on the

206   method of Cazorla et al. (2013), which used sun photometer measurements to arrive at the following classifications

207   as part of evaluating aircraft data over California, USA: coated large particles, dust and elemental carbon mix, dust

208   dominated, organic carbon and dust mix, organic carbon dominated, elemental carbon and organic carbon mix, mixed,

209   and elemental carbon dominated. This method has been used for cases when chemical composition is not available

210   (Höpner et al., 2019), and can be useful because the composition data from the AMS is limited to submicrometer

211   particles (0.06 to 0.6 µm vacuum aerodynamic diameter) while the f(RH) includes relatively larger particles (< 5 µm

212   dry diameter).

213

214   **2.2.5 Effective Particle Density**

215   Following Shingler et al. (Shingler et al., 2016b), effective particle density was calculated by dividing the sum of the

216   30 s total mass concentration from the AMS species (organics, SO$_4^{2-}$, NO$_3^-$, NH$_4^+$, and Cl$^-$) and 30 s averaged black

217   carbon from SP2 by the 30 s averaged integrated (for particles with diameter from 0.1 to 1 µm) volume concentration

218   from the LAS (Table 21).

219

220   **2.3 Modeling**

221

2.3.1 Trajectory Analysis

This work leverages trajectory results explained in detail by Hilario et al. (2021) using the National Oceanic and Atmospheric Administration (NOAA) Hybrid Single Particle Lagrangian Integrated Trajectory Model (HYSPLIT) (Stein et al., 2015; Rolph et al., 2017). Five-day HYSPLIT back trajectories from specific CAMP[2]Ex flight locations were associated with air masses undergoing long-range transport from either the Maritime Continent (MC), East Asia (EA), peninsular Southeast Asia (PSEA), or the West Pacific (WP) when they were within the regions at altitudes below 2 km for more than 6 h. The back trajectories were generated based on 1-minute resolution aircraft locations and 0.25° x 0.25° resolution NOAA Global Forecasting System (GFS) archived meteorological data. The source regions are approximately within the following lowest and highest latitude and longitude values, respectively: MC (-9.5° - 6.5° and 95° - 119°), EA (22° - 47° and 105° - 121.5°), PSEA (10° - 20° and 98° - 106 °), and WP (3°-25° and 120.5°-122.5°). The classification "Other" was used for back trajectories that either passed by the regions but at elevations above the boundary layer (defined as 2 km), came from sources farther away than the four listed above, were more localized to the Philippines, had too few sample counts, or were from stagnant air (Hilario et al., 2021).

2.3.2 CAM-chem Model Configuration

The Community Atmosphere Model with comprehensive tropospheric and stratospheric chemistry CAM-chem is used here as the atmospheric component of the Community Earth System Model (CESM2). CAM-chem includes the modal aerosol model (MAM4) (Liu et al., 2016) and results were evaluated with the CAMP[2]Ex AMS composition and f(RH) observations for two case studies. Two CAM-chem simulations with different horizontal resolutions were performed using the spectral element grid mesh and dynamical core. The grid mesh resolution for one simulation was uniform with ~111 km (labeled ne30). The other simulation employed regional refinement over East Asia with grid spacing ~27 km (labeled MUSICA) in the regionally refined region and ~111 km elsewhere across the globe; a configuration as part of the Multi-Scale Infrastructure for Chemistry and Aerosols version 0 (MUSICAv0) (Schwantes et al., 2022). More information about CAM-chem is in the supplementary section (S1).

In CAM-chem, aerosol hygroscopicity is represented with the kappa value (Petters and Kreidenweis, 2007) using the mixing rule (Stokes and Robinson, 1966). Kappa was calculated from the CAM-chem Aitken (0.015 – 0.053 µm) and accumulation mode (0.058 – 0.48 µm) outputs based on the volume fractions of the aerosol constituents (ε, Eq. 3) that were derived from their densities (Table S1). The following internally mixed aerosol species from CAM-chem were included in the analysis: organics (primary/hydrophobic, aged/hygroscopic, and secondary ($C_{15}H_{38}O_2$)), sulfate (NH_4HSO_4), sea salt, dust ($AlSiO_5$), and black carbon (primary/hydrophobic and aged/hygroscopic) (Tilmes et al., 2023). Some limitations in the calculation of kappa are that CAM-chem does not include nitrate aerosol, and that constant kappa values for primary and aged organics based on past work (Table S1) were used, even if it is known that kappa of organics varies with aging (Kuang et al., 2020). Kappa was also calculated from the submicrometer AMS and SP2 observations using the assigned species properties for available aerosol species in CAM-chem: aged organics, aged black carbon, and ammonium sulfate. Submicrometer sea salt and dust data are not available and were not included in the calculation for submicrometer kappa from observations.

$$\kappa_{chem} = \sum \kappa_i \, \varepsilon_i \qquad\qquad (3)$$

To enable a corresponding evaluation based on actual aerosol hygroscopicity observations, the f(RH) from CAMP²Ex were converted to kappa based on past studies (Brock et al., 2016b; Kuang et al., 2017; Van Diedenhoven et al., 2022). The approximate wet (80% %) and dry (20% %) relative humidity values of the scattering measurements were used to convert f(RH) to an optical kappa (κ_{opt}) based on Equation 4 (Brock et al., 2016b; Kuang et al., 2017). This was approximated from the proportional relationship between the aerosol scattering cross section (which is the basis of f(RH)) and aerosol volume (the change of which is usually described as growth factor) which Brock et al. (2016b) in their study had associated with kappa. The optical kappa was converted to the chemical kappa (κ_{chem}) based on the slope of the relationship between κ_{opt} and κ_{chem} from Brock et al. (2016b). This method (Eq. 5) of converting κ_{opt} to κ_{chem} was also used by van Diedenhoven et al. (2022) for the f(RH) data for CAMP²Ex and is associated with 40% % uncertainty (Van Diedenhoven et al., 2022). The derived chemical kappa values for bulk aerosol particles are compared to the kappa calculated using the ZSR mixing rule from the submicrometer observations (AMS and SP2) and model outputs.

$$f(RH) = \frac{1 + \kappa_{opt} \frac{RH_{wet}}{100 - RH_{wet}}}{1 + \kappa_{opt} \frac{RH_{dry}}{100 - RH_{dry}}} \qquad\qquad (4)$$

$$\kappa_{chem} \approx \frac{\kappa_{opt}}{0.56} \qquad\qquad (5)$$

3. Results and Discussion

3.1 General Characterization of f(RH) for CAMP²Ex

3.1.1   Spatial Distribution of f(RH)

The f(RH) values in the CAMP²Ex campaign (Fig. 1a) had an interquartile range of values between 1.05 and 1.42 and were low (median of 1.24 for 143,107 1 s points) compared to other (Table 1) (Table 2) polluted marine environments (Titos et al., 2021). We note that the comparisons to other studies may be affected by the slight difference in relative humidity (f(RH=85% %/RH=40% % for Titos et al. (2021) and f(RH=82 ± 10% %/RH<40% % for this study) used to calculate f(RH). The distribution of f(RH) and ambient RH values is narrowest in the lowest altitudes (< 3 km), where most of the samples were taken (Fig. 1b). Both f(RH) and ambient RH distributions become broader at higher altitudes, where there is a higher prevalence also for higher f(RH) values and lower ambient RH values. Broadening of the f(RH) distribution at higher altitudes is at least partially attributed to lower dry scattering coefficients that result in increased uncertainty in the calculation of f(RH). The different aerosol sources (Fig. 1a) in the region also contribute to the range of measured f(RH), with transported emissions from more distant sources presumably more influential at the highest altitude ranges.

288
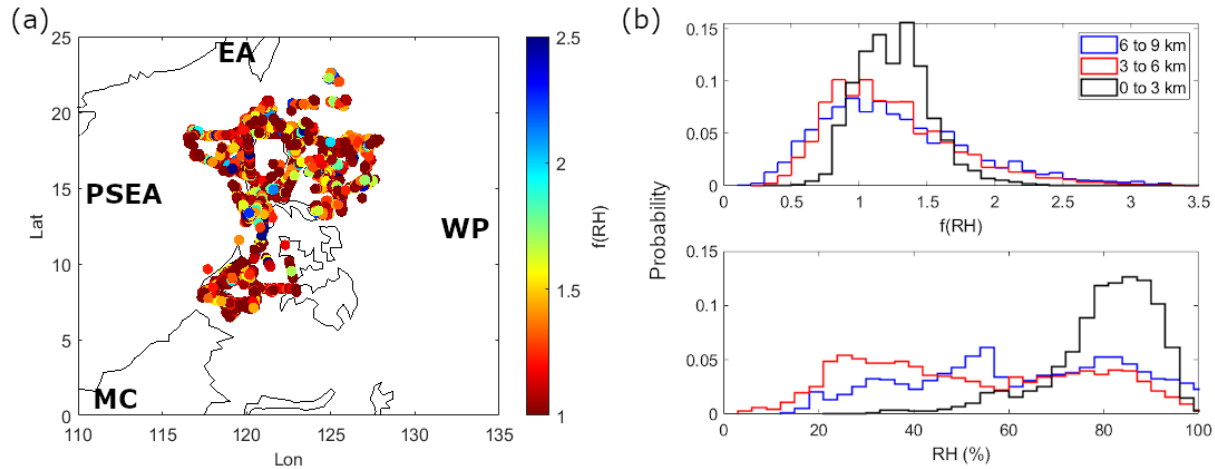
Figure 1. (a) Map showing flight locations during CAMP²Ex color coded by f(RH=82 % ± 10 %/RH<40 %) 1 s values at 550 nm and approximate locations of the air mass sources (black text) identified by Hilario et al. (2021) that affected CAMP²Ex: Maritime Continent (MC), East Asia (EA), peninsular Southeast Asia (PSEA), and the West Pacific (WP) (PSEA is farther west at ~105°E and EA extends farther north) of air mass sources (Hilario et al., 2021) around the region. (b) Histograms of f(RH=82 % ± 10 %/RH<40 %) at 550 nm and ambient relative humidity (RH) for three altitude bins with the following counts: $n_{(0 \text{ to } 3 \text{ km})}$: 139,026, $n_{(3 \text{ to } 6 \text{ km})}$: 10,321, and $n_{(6 \text{ to } 9 \text{ km})}$: 7,260.

The lowest median f(RH) (1.05 with Q1 and Q3 of 0.94 and 1.2) is from air masses traced to the MC (Fig. 2a), which coincide with influence from smoke particles, similar to values recorded in past studies from aged biomass (Table 2). The air mass from EA (Fig. 2a) has the narrowest range of values (Q1: 1.28, median (Q2): 1.38, Q3: 1.47) compared to other air masses, likely representative of urban aerosol particles (Table 2). The highest median f(RH) (1.49 with Q1 and Q3 of 1.26 of 1.73) are from air masses with back trajectories from the WP (Fig. 2a), likely due to marine aerosol particles interacting with particles from the MC and other regional sources. This mixing of the otherwise clean marine air with regional pollution sources effectively decreases aerosol hygroscopicity and this type of environment is often called a polluted marine environment (Titos et al., 2021).

Table 12: Hygroscopicity values of various aerosol types based on selected summary studies for measured g(RH) (Swietlicki et al., 2008)(Swietlicki et al., 2008) and f(RH) (Burgos et al., 2019; Titos et al., 2021)(Eldering et al., 2002; Doherty et al., 2005; Liu and Li, 2018; Dumka et al., 2017; Gogoi et al., 2015; Burgos et al., 2019; Titos et al., 2021), and modeled κ (Pringle et al., 2010)(Pringle et al., 2010), and measured f(RH) for identified air masses affecting CAMP²Ex (Hilario et al., 2021): Maritime Continent (MC), East Asia (EA), peninsular Southeast Asia (PSEA), West Pacific (WP), and Other, categorized by associated aerosol source.

Aerosol Type	Past Studies		κ**** (5 - 500 nm)	Air Masses Affecting CAMP²Ex
	g(RH=90%)* (10 - 500 nm)	f(RH=85%/RH=40%)** (< 1000 nm)		f(RH=82 ± 10 %/RH<40%)** (< 5000 nm)
Clean Marine	1.62 - 2.14	2.10 - 2.30	0.92	1.49 (WP)
Polluted Marine	1.00 - 1.76	1.73 - 2.20	0.59	1.23 (Other)
Urban Continental	1.00 - 1.68	1.38 - 1.60	0.21 - 0.36	1.20 - 1.38 (EA, PSEA)
Aged Biomass	1.15 - 1.30	1.02 - 2.1***	< 0.1	1.05 (MC)

*Mean values from various ground-based sites
**Median values
***Gomez et al., 2018 mean (f(RH=85%/RH=25%))
****Mean surface values

309   Most (98% %) of the f(RH) data were calculated for observations below 3 km (Fig. 2b), due to the relatively clean

310   free troposphere in the region. Median f(RH) values generally decrease with altitude in the lower 3 km. An increase

311   in median f(RH) is observed between 4 – 6 km (median from 1.14 to 1.32), where the contribution of the mixed air

312   mass ("Other") is most dominant. The f(RH) values decrease above 6 km to the lowest median f(RH) (1.07) between

313   8 – 9 km, where air masses are generally from Other and the MC.

314   Latitudinally (Fig. 2c), f(RH) is lowest nearest Borneo in the MC (median of 0.95 to 1.07 in the regions from 6.85° N

315   – 10.25° N), coincident with the dominant influence of biomass burning. There were active fires in the area during the

316   time samples were taken from this latitude. f(RH) is highest in the northern Philippines (median of 1.33 to 1.44 in the

317   regions from 18.75° N – 22.15° N), where the influence of WP and EA air was most prevalent. This is consistent with

318   the longitude data (Fig. 2d), which exhibit the lowest f(RH) values for longitudes (median of 1.02 to 1.18 in the regions

319   from 117.95° E – 120.55° E) that had the highest MC contribution. The highest f(RH) is observed in longitudes

320   (median of 1.38 to 1.40 in the regions west of 116.65° E and east of 123.15° E) that were more associated with the

321   northern Philippines (Fig. 1a). To delve deeper into our analysis, we discuss next the size and composition data.

322

323
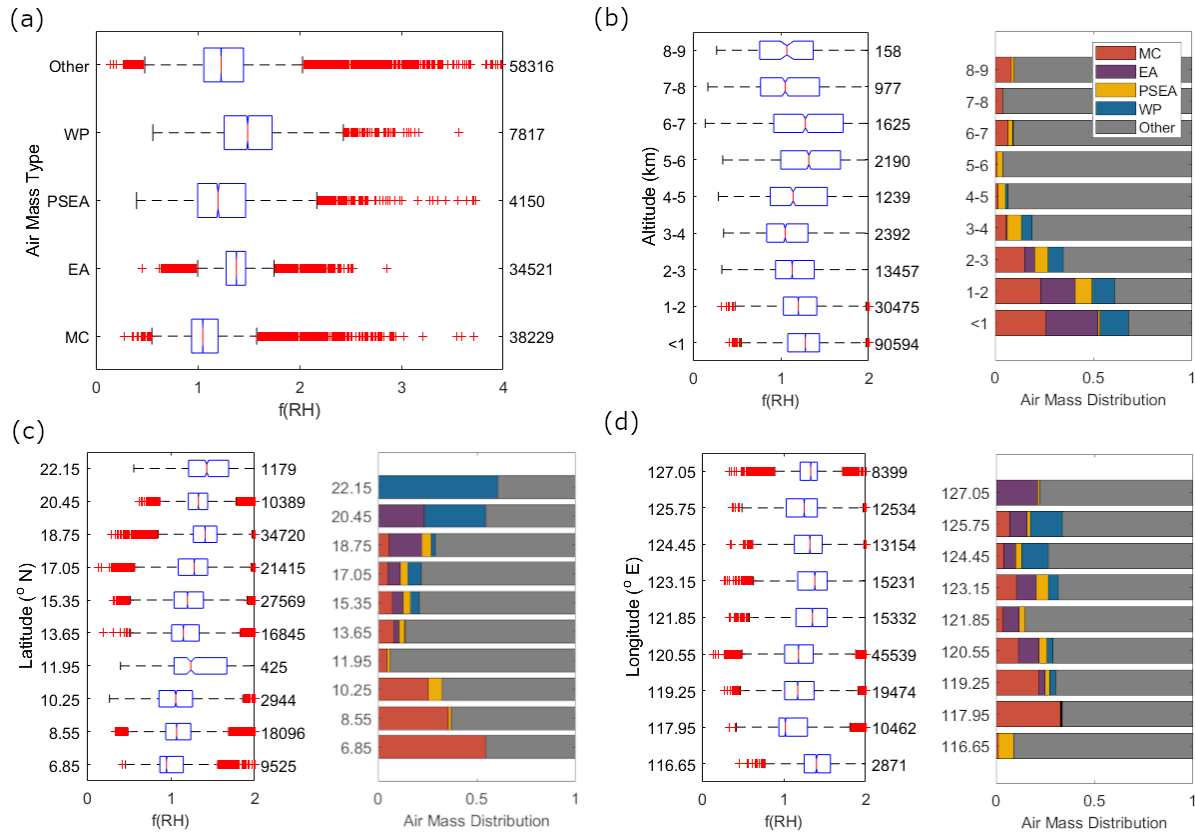
324 **Figure 2. Distribution of ~~1-s~~ _f_(RH=82 % ± 10 %/RH<40 %) 1 s data at 550 nm during the CAMP²Ex field campaign for**
325 **relevant (a) air masses, (b) altitude, (c) latitude, and (d) longitude levels and corresponding stacked bars of air mass**
326 **contributions for panels b - d. The (a) air mass types are from Hilario et al. (2021). The numbers to the right of the notched**
327 **boxplots (boxes correspond to the 25th to 75th percentile of the data, the red line is the 50th percentile, the whiskers represent**
328 **1.5 * the interquartile range, the red crosses are the outliers, and when the notches in the boxplots do not overlap there is**
329 **95 % confidence that the medians of the boxplots are different) are the counts, and the (b – d) bars to the right of the**
330 **boxplots show the fractional contribution of each air mass type to the total number of air masses in the specific location.**
331 **The y-values for (c-d) latitude and longitude are the midpoints of the specific coordinate bins.**

3.1.2 _f_(RH) Relationships with Size and Composition

333 The relative size of particles per air mass can be inferred from the extinction Ångström exponent (AE), which relates

334 the extinction of light at specific wavelengths to particle size (Ångström, 1929). Since scattering is the dominant

335 component of extinction, the scattering Ångström exponent (SAE) is often used to relate to particle size, where larger

336 SAE suggests smaller particles. The median SAE values (Fig. 3a) are similar and between 2.09 (MC with Q1 and Q3

337 of 1.92 and 2.26) to 2.16 (Other with Q1 and Q3 of 1.75 and 2.32) for four of five air masses, indicative of smaller

338 particles. The WP has a median value of 1.37 (with Q1 and Q3 of 1.05 and 1.88), suggestive of the presence of a

339 mixture of accumulation-mode and coarse-mode particles (SAE < 1 occurs for large particles like sea salt and dust)

340 (Schuster et al., 2006; Bergstrom et al., 2007). Past studies have suggested that biomass burning particles exhibit SAE

341 values greater than 1.4, which does not discount the fact that most of the _f_(RH) data collected during CAMP²Ex are

342 possibly impacted by biomass burning.
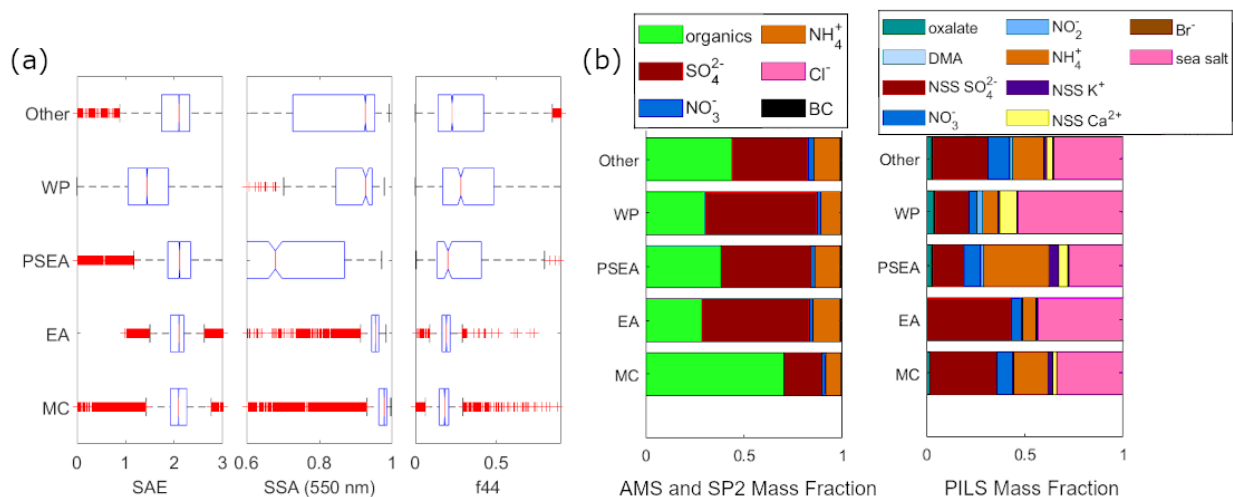
Figure 3. Physicochemical properties of air masses. (a) Boxplots (boxes correspond to the 25th to 75th percentile of the data, the red line is the 50th percentile, the whiskers represent 1.5 * the interquartile range, the red crosses are the outliers, and when the notches in the boxplots do not overlap there is 95 % confidence that the medians of the boxplots are different) of ~~1 s~~**scattering Ångström exponent (SAE), single scattering albedo (SSA, 550 nm), and ratio of the mass spectral marker m/z 44 marker relative to total organic mass (f44) and (b) (left) submicrometer mean aerosol mass spectrometer (AMS) derived organic, SO₄²⁻, NO₃⁻, NH₄⁺, and Cl⁻,** ~~and~~ **soot photometer (SP2) derived black carbon (BC) mass fractions and (right) bulk (< 5 μm) mean particle-into-liquid sampler (PILS) and ion chromatograph derived oxalate, dimethylamine (DMA), non-sea salt SO₄²⁻, NO₃⁻, NO₂⁻, NH₄⁺, non-sea salt K⁺, non-sea salt Ca²⁺, Br⁻, and sea salt mass fractions per air mass: Maritime Continent (MC), East Asia (EA), Peninsular Southeast Asia (PSEA), West Pacific (WP), and Other (Hilario et al., 2021).**

One of the indicators of biomass burning in Southeast Asia is organic matter (Adam et al., 2021). The MC air mass (Fig. 3b) has the greatest (71~~%~~ %) mass fraction of organics among the air masses and the highest median SSA (0.98 with Q1 and Q3 of 0.96 and 0.99) (Fig. 3a) that suggests more scattering, rather than absorbing, particles (Moosmüller and Sorensen, 2018). This is consistent with observations from field work in tropical peatland fire in Southeast Asia, where particles were mostly from smoldering combustion and were moderately absorbing, with brown carbon dominating absorbance (Stockwell et al., 2016). Smoldering combustion, which is more common in the Maritime Continent (Reid et al., 2013), is known to produce less elemental carbon (Reid et al., 2005) and potassium (Robinson et al., 2004) compared to flaming combustion. Biomass burning activities were active in the MC during the field campaign (Reid et al., 2023). The MC air mass also has the lowest f_{44} median values (0.18 with Q1 and Q3 of 0.15 and 0.21) (Fig. 3a) suggesting it is the least-oxidized and least photochemically-aged air mass and thus closest to the source compared to other air masses. Chen et al. (2022) who studied tropical peat smoldering (similar to those in MC) showed that primary organics were not oxidized ($f_{44} < 0.02$) while secondary organics were highly oxidized, that oxidation increases f_{44} (oxidized organics: $0.01 < f_{44} < 0.11$), and that high RH speeds up the oxidation process especially for smaller particles (~100 nm) (Chen et al., 2022). In the U.S., as another example, f_{44} from wildfire plumes up to 8 hours old did not exceed 0.12 (Garofalo et al., 2019). The high RH during CAMP²Ex (Fig. 1b) likely led to the increased oxidation of secondary organics resulting in median f_{44} values that are relatively high (for all air masses even in MC), suggesting that most of the particles sampled during CAMP²Ex are aged. The high organic mass fraction is consistent with the MC having the lowest median f(RH) as organics are known to reduce aerosol hygroscopicity (Kalberer, 2014; Sorooshian et al., 2017; Shingler et al., 2016a).

372 There is an inverse relationship between hygroscopicity and organic mass fraction data that is most evident in f(RH)

373 values collected within the boundary layer (< 3 km) during CAMP²Ex (Fig. 4a). Those data points that have the highest

374 organic mass fraction values (> 0.6) are also associated with CO concentrations (> 250 ppb) that are typically

375 associated with biomass burning (Shingler et al., 2016a) and are mostly from the MC area (Fig. 4b). The relationship

376 between f(RH) and organic mass fraction during CAMP²Ex is similar to those in the Indian ocean during INDOEX

377 (based on the sloped of calculated f(RH) from estimated γ and organic mass fraction) (Quinn et al., 2005), which is

378 similarly affected by the outflow of biomass burning. The slope of the inverse relationship between f(RH) and organic

379 mass fraction is most steeply negative (-0.81) for the air masses coming from EA (Fig. 4c). This slope for the air

380 masses coming from EA is less steep than the f(RH=85 %/RH=40 %) at 550 nm to organic mass fraction relationship

381 (-1.20 ± 0.04) from a ground station in the populated and growing region of the Yangtze River Delta in China (Zhang

382 et al., 2015), where organic contributions are lower and mean f(RH) values are higher (1.58 ± 0.12) than the median

383 f(RH) (1.38) during CAMP²Ex for air massed coming from EA.

384
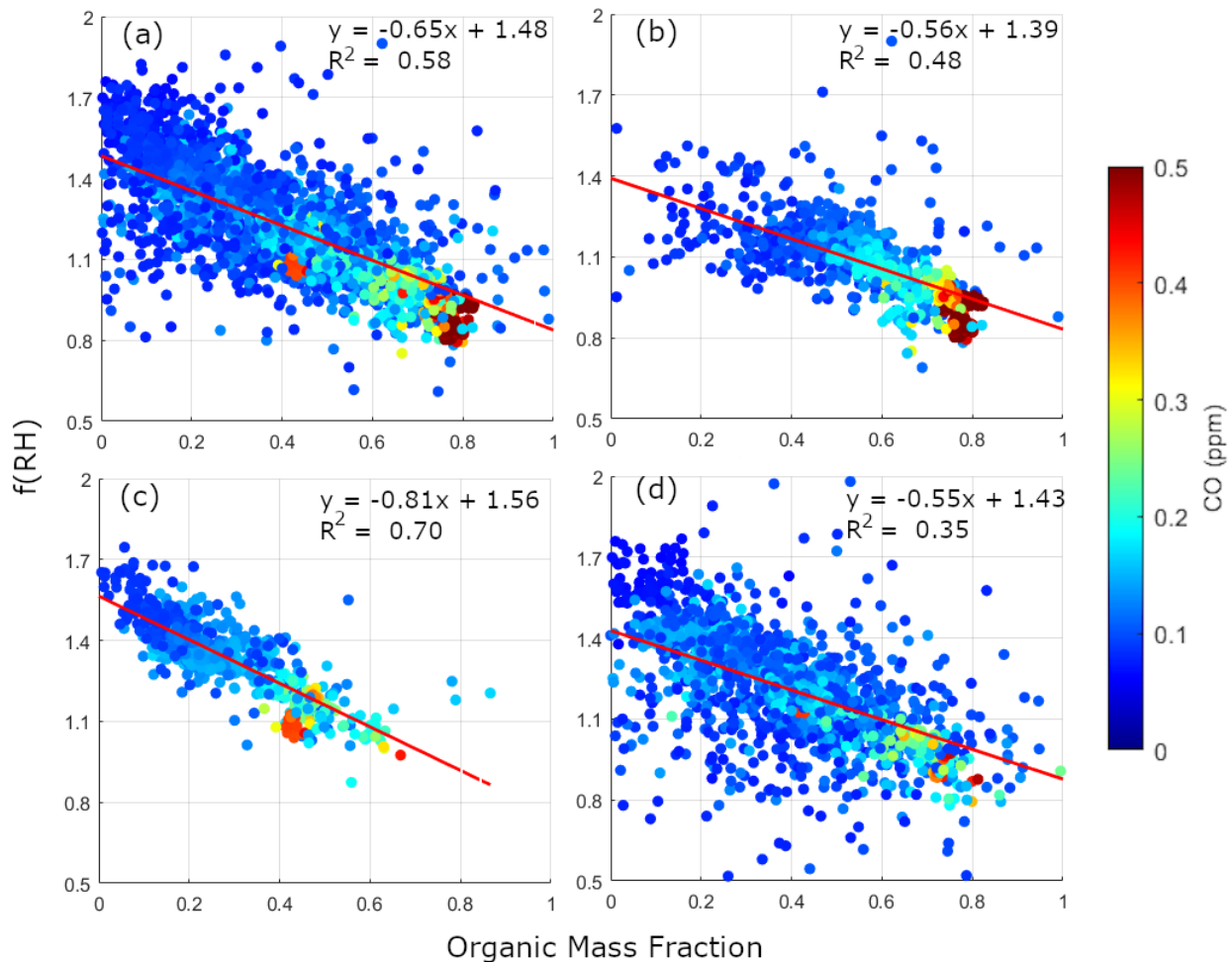
385 **Figure 4. Effect of organic mass fraction on f(RH).** (a-d) Scatter plots of 30 s averaged f(RH=82 % ± 10 %/RH<40 %) at
386 550 nm and corresponding organic mass fraction contribution to total submicrometer aerosol mass (sum of organic, SO₄²⁻,
387 NO₃⁻, NH₄⁺, Cl⁻, and black carbon (BC) mass concentration) and (red) linear regression line and (upper right)

388 **corresponding equation and goodness of fit for (a) all data collected at altitudes below 3 km and (b-d) for air masses coming**
389 **from (b) the Maritime Continent (MC), (c) East Asia (EA), and (d) Other. The dots are colored by their CO concentration.**

390 The highest median f(RH) values are from the WP and EA air masses (Fig. 2a). Both have lower organic mass
391 fractions (0.29 and 0.30, respectively) compared to other air masses and are therefore expected to have higher f(RH)
392 based on Fig. 4. The WP air masses have coarser particles, based on their SAE values (Fig. 3a), and have a marine
393 origin (with higher DMA mass fraction, Fig. 3b) with high sea salt fraction (54~~%~~ %, Fig. 3b), contributing to it having
394 the highest median f(RH) amongst the air masses. The WP air masses appear to have interacted with aged organic
395 particles from biomass burning and industry including fine absorbing particles potentially from industry and dust
396 owing to its relatively high median f_{44} (0.26 with Q1 and Q3 of 0.17 and 0.48) and low median SSA (0.93 with Q1
397 and Q3 of 0.85 and 0.95). Particles with predominantly clean marine sources tend to have higher ($\geq$ 0.97) SSA
398 (Dubovik et al., 2002), thus the WP data suggest a polluted marine source (Lacagnina et al., 2015). Though, we note
399 that the air masses from the WP have relatively low scattering and absorption coefficients and that these could have
400 affected the calculations for SSA. EA air exhibits the highest non-sea salt sulfate mass fraction (0.43) (Fig. 3b) that,
401 along with its predominantly fine particle size and median SSA (0.95 with Q1 and Q3 of 0.94 and 0.96), strongly
402 suggests that it was transported from an urban source. Sulfate is a known industrial product of East Asia (Smith et al.,
403 2011; Li et al., 2017; Lorenzo et al., 2023).

404 Particles from PSEA have the lowest median SSA (0.68 with Q1 and Q3 of 0.55 and 0.87) (Fig. 3a). This suggests the
405 presence of more absorbing particles relative to scattering, possibly including elemental carbon and aged dust. Based
406 on the PSEA air masses having the highest non-sea salt potassium mass fraction (0.05, Fig. 3b) the particles could be
407 from biomass burning. It is well-documented that dust can be entrained in smoke plumes due to reasons such as
408 turbulent mixing around flames and burn fronts (Palmer, 1981; Kavouras et al., 2012; Maudlin et al., 2015; Schlosser
409 et al., 2017). Dust from East Asia and biomass burning from PSEA have been observed to be mixed in the boreal
410 spring in Taiwan (Dong et al., 2018), and though CAMP[2]Ex sampled during a different season, it is still possible that
411 this mixing of East Asian dust and PSEA biomass burning could have occurred and impacted the CAMP[2]Ex region
412 during the field campaign.

413
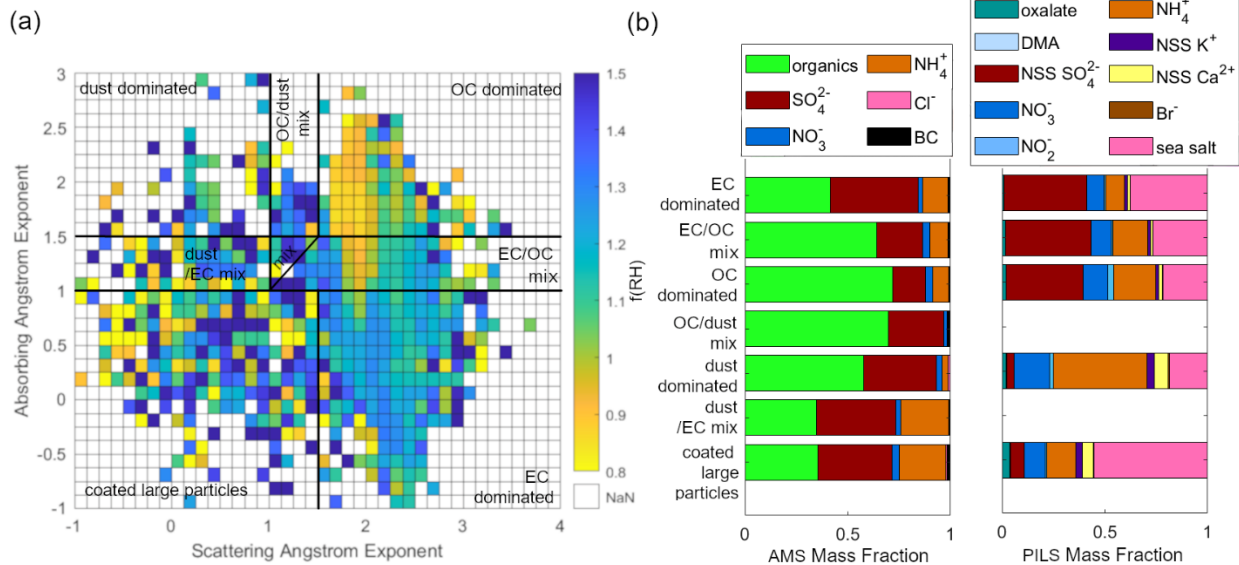
Figure 5. Aerosol types based on particle optical data. (a) Median *f*(RH =82 % ± 10 %/RH<40 %) at 550 nm of data points
with absorbing Ångström Exponent (AAE, 470-660 nm) and scattering Ångström Exponent (SAE, 450-700 nm) values that
correspond to suggested aerosol types from past studies (Cazorla et al., 2013) with following counts and bulk median
f(RH=82 % ± 10 %/RH<40 %) per aerosol type: EC dominated (16,908 and 1.19), EC/OC mix + mix (20,686 and 1.03), OC
dominated (1942 and 0.94), OC/dust mix (55 and 1.31), dust dominated (79 and 1.15), dust/EC mix (204 and 1.12), and
coated large particles (729 and 1.21). **(b) (left)** Submicrometer mean organic, SO$_4$$^{2-}$, NO$_3$$^-$, NH$_4$$^+$, Cl$^-$, and black carbon (BC)
mass fractions and **(right)** available bulk (< 5 µm) oxalate, dimethylamine (DMA), non-sea salt SO$_4$$^{2-}$, NO$_3$$^-$, NO$_2$$^-$, NH$_4$$^+$,
non-sea salt K$^+$, non-sea salt Ca^{2+}, Br$^-$, and sea salt mass fractions per aerosol type.

Using the AAE and SAE with categorization determined by Cazorla et al. (2013), the *f*(RH) can be related to the types

of aerosols. Note that the median *f*(RH) values for the aerosol types may be slightly different than the raw 1 s *f*(RH)

data because the median *f*(RH) is only calculated for the aerosol types when both the scattering and absorbing

Ångström Exponent values are available. The highest median *f*(RH) of 1.31 (with Q1 and Q3 of 0.89 and 1.46) and

1.21 (with Q1 and Q3 of 0.88 and 1.68) are from the OC/dust mix and coated large particles aerosol types (Fig. 5),

respectively, though there are only 55 data points for the OC/dust mix so the aerosol classification for it may not be

as robust. The high *f*(RH) for the coated large particles is consistent with its largest bulk sea salt mass fraction (0.56)

(Fig. 5b) compared to other aerosol types, though they only make up 1.8 % of the total number of particles. Dust

dominated particles make up only 0.05<s>%</s> % of the total number of particles and had the highest non-sea salt calcium

and a median *f*(RH) of 1.15 (with Q1 and Q3 of 0.94 and 1.43).

Most of the aerosol particles (< 5 µm dry diameter and 93<s>%</s> % of all particles) collected during the CAMP^{2}Ex field

campaign have optical properties (Fig. 5a) that resembled EC/OC mix + mix (in this case we combined the sub-

categories of EC/OC mix and mix) (51<s>%</s> %) and EC dominated (42<s>%</s> %) aerosol types. These carbonaceous particles

are less hygroscopic, and their dominance helps to explain the low median *f*(RH) in the CAMP^{2}Ex region. The EC

dominated particles have the third highest median *f*(RH) at 1.19 (with Q1 and Q3 of 1.05 and 1.33), which is unusual

because EC is known to be hydrophobic. Compositional data sheds some light on this, because the particles classified

as EC dominated have higher submicrometer sulfate (0.43) and bulk sea salt (0.38) mass fractions (Fig. 5b) compared

to particles classified as OC (0.16 and 0.22) and dust dominated (0.35 and 0.19), which are known to have low

440   hygroscopicity in general. This mixing of sulfate and sea salt with EC dominated particles increases their bulk *f*(RH).

441   The EC dominated particles come from the EA, MC, and Other air masses. East Asia is a known sulfur source and

442   shipping contributes to sulfate in the region (Miller et al., 2023). Peat smoke particles from MC have also been found

443   in past studies to have sulfate mixed with carbonaceous species (Nakajima et al., 1999), where up to ~20~~%~~ % of the

444   mass fraction of secondary organic aerosol from lab experiments on peat burning was attributed to sulfate (Chen et

445   al., 2022).

446   The OC dominated type has the highest submicrometer organic mass fraction (0.72) and a median *f*(RH) of 0.94 (with

447   Q1 and Q3 of 0.85 and 1.06), which is consistent with the expected effect of organics to lower hygroscopicity. The

448   median *f*(RH) values below 1, though, are counterintuitive given that the presence of moisture in the region is thought

449   to generally increase the particle size and consequently the amount of aerosol light scattering. Data where *f*(RH) is

450   less than unity have been observed in past studies due to a number of suspected factors including (but not limited to)

451   volatilization effects, changes in optical properties during humidification, and particle restructuring (Shingler et al.,

452   2016b).

453

454
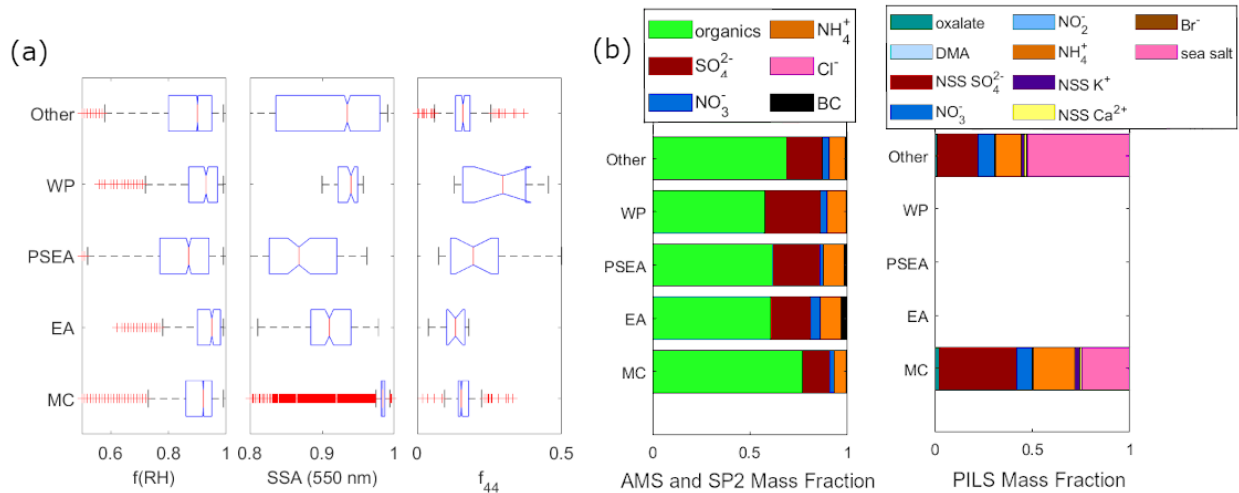
455   **Figure 6. Physicochemical properties of air masses with sub-1 *f*(RH) at 550 nm. (a) Boxplots (boxes correspond to the 25th**
456   **to 75th percentile of the data, the red line is the 50th percentile, the whiskers represent 1.5 * the interquartile range, the red**
457   **crosses are the outliers, and when the notches in the boxplots do not overlap there is 95 % confidence that the medians of**
458   **the boxplots are different) of 1 s *f*(RH=82 % ± 10 %/RH<40 %) < 1 (MC: 14,612, EA: 473, PSEA: 986, WP: 483, and Other:**
459   **9919 counts) and the corresponding single scattering albedo (SSA, 550 nm) and ratio of the mass spectral marker m/z 44**
460   **marker relative to total organic mass (f_{44}) and (b) (left) submicrometer mean organic, SO_4^{2-}, NO_3^-, NH_4^+, Cl^-, and black**
461   **carbon (BC) mass fractions and (right) available bulk (< 5 μm) oxalate, DMA, non-sea salt SO_4^{2-}, NO_3^-, NO_2^-, NH_4^+, non-**
462   **sea salt K^+, non-sea salt Ca^{2+}, Br^-, and sea salt mass fractions per regional air mass (Hilario et al., 2021) for times with**
463   ***f*(RH=82 % ± 10 %/RH<40 %) < 1.**

464   To investigate aerosol characteristics when *f*(RH) is < 1, we plot the f(RH) box plots from each of the regions for data

465   points where *f*(RH) < 1 (Fig. 6a). There are several instances (26,473 times or 19~~%~~ % of the time for the whole

466   campaign) when the *f*(RH) was below 1. In general, 30 s resolution organic mass fractions greater than 0.75 correspond

467   to sub-1 *f*(RH) (Fig. 4a). The most prevalent regional air mass association for sub-1 *f*(RH) is with the MC air masses

468 (*f*(RH) < 1 from the MC was 56~~%~~ % of all data). The mean organic mass fraction is dominant (0.57 – 0.77) and almost

469 doubled compared to the whole campaign (Fig. 3b), for all the air masses with sub-1 *f*(RH) (Fig. 6b). Mean organic

470 mass fraction is highest for the MC (0.77) air mass. The organics from the sub-1 *f*(RH) data are the least aged

471 throughout the campaign for the MC, PSEA, and Other air masses (Fig. 6a). The CAMP^{2}Ex data offer an opportunity

472 to inspect the prevalence of such values and to see what factors coincide with such situations. However, the unique

473 sample make-up of the particles in the CAMP^{2}Ex region makes other reasons, including sample losses due to

474 volatilization, also plausible (Reid et al., 2023). Shingler et al. (Shingler et al., 2016b) also observed such sub-1 values

475 for both *f*(RH) and the humidified diameter growth factor g(RH) in air masses enriched with carbonaceous components

476 over North America.

477 The most dominant aerosol types for the sub-1 *f*(RH) data are the carbonaceous ones (96~~%~~ %) (Fig. 5b), with the

478 EC/OC component contributing the most: EC/OC mix + mix (the combined sub-categories of EC/OC mix and mix)

479 (68~~%~~ %), EC-dominated (18~~%~~ %), and OC-dominated (10~~%~~ %). Both bulk ammonium and sulfate mass fractions for

480 the MC also are higher for the sub-1 *f*(RH) cases (Fig. 6b) compared to the whole campaign (Fig. 3b, PILS), while the

481 bulk sea salt mass fraction was lower. The bulk sea salt mass fraction of the Other category (Fig. 6b) increases for the

482 sub-1 *f*(RH). Most of the particles contributing to the sub-1 *f*(RH) are fine particles (median Ångström Exponent ~2,

483 Fig. 6a) with more reflective characteristics (SSA ≥ 0.90) compared to data for the entire campaign. To understand

484 more about sub-1 *f*(RH), we will look at a selected case in the succeeding section.

485 **3.2 Case Studies**

486 **3.2.1 Sub-1 *f*(RH) from Biomass Burning Smoke**

487 The chosen case study is part of a flight on 16 September 2019 that occurred closest to the Maritime Continent, which

488 is the source of the air masses that had the most counts of sub-1 *f*(RH) (Section 3.1.2). This flight coincided with an

489 active biomass burning event on 14 September 2019 (Nasa, 2020) and fire hotspots in the Maritime Continent were

490 numerous throughout September 2019 (Othman et al., 2022). The back trajectories at 01:00 UTC, when the aircraft

491 began to make measurements closest to the surface (~300 m altitude) and perpendicular to the wind, all come from

492 the southwest of the aircraft location (Fig. 7a), in the direction from where biomass burning emissions were being

493 transported. Details about the flight and conditions during this case study are found in Crosbie et al. (2022). In their

494 study they note the smoke to be from Kalimantan with an age between 48 and 72 h. Consistently low *f*(RH) (all below

495 1, Fig. 7b) values were observed for a little less than an hour, until the aircraft began its ascent (Fig.7b). The aerosol

496 mass concentrations of >70 µg m^{-3} were among the highest in the entire field campaign and were dominated by

497 organics (Fig. 7b).
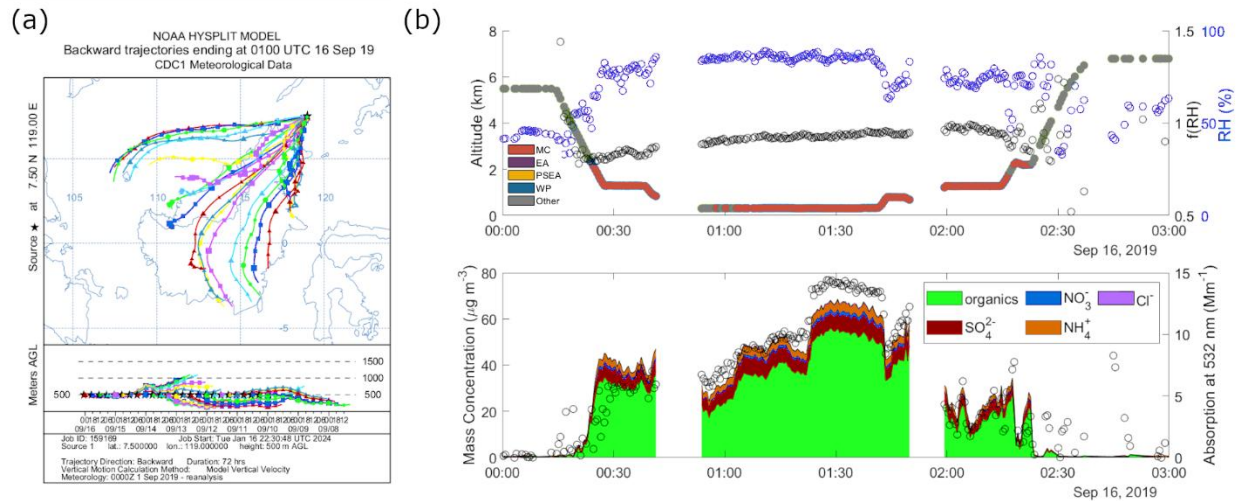
Figure 7. Case study of sub-1 *f*(RH=82 % ± 10 %/RH<40 %) at 550 nm on 16 September 2019. (a) Five-day back trajectories at the approximate flight location at 01:00 UTC. (b) (top) Time series plots of altitude colored by regional air mass, *f*(RH) in black circles, and RH (blue circles), and (bottom) aerosol mass concentrations from the AMS and absorption at 532 nm (black circles) during one of the flight legs closest to the surface from 00:00 to 03:00 UTC.

The sub-1 *f*(RH) during the lowest altitudes of the aircraft, from 01:00 to 01:40 UTC, are correlated with approximations of the submicrometer particle effective density (Fig. 8a). Absorption measurements along with back trajectories linked to active fires point to the increasing presence of EC and brown carbon with increasing particle density (even if there were no valid EC measurements for this specific time). Submicrometer number concentration, dry absorption (532 nm), organic mass fraction, and single scattering albedo are highest for the smallest effective density values for sub-1 *f*(RH) (Fig. 8b) during the entire campaign, likely due to the presence of EC and OC. This is consistent with the most dominant aerosol type during the field campaign, which is a mix of elemental and organic carbon based on SAE and AAE values. The dataset cannot be used to prove particle restructuring and very likely the sub-1 *f*(RH) values are due to other factors since particles' history included passes through humid areas where restructuring presumably would have already occurred prior to reaching the aircraft. In addition, smoldering from peat, which is dominant in the MC fires (Reid et al., 2023), is known to produce homogenous spheres, with no voids, that are similar to OC particles (Pokhrel et al., 2021), making restructuring unlikely to be the dominant mechanism to explain our findings. However, we present these results for the sake of documenting a Southeast Asia case of these unusual events occurring in EC/organic-rich air masses similar to past work (e.g., Shingler et al., 2016b and references therein) to emphasize that these events occur throughout the world and to motivate more research into the matter.

518
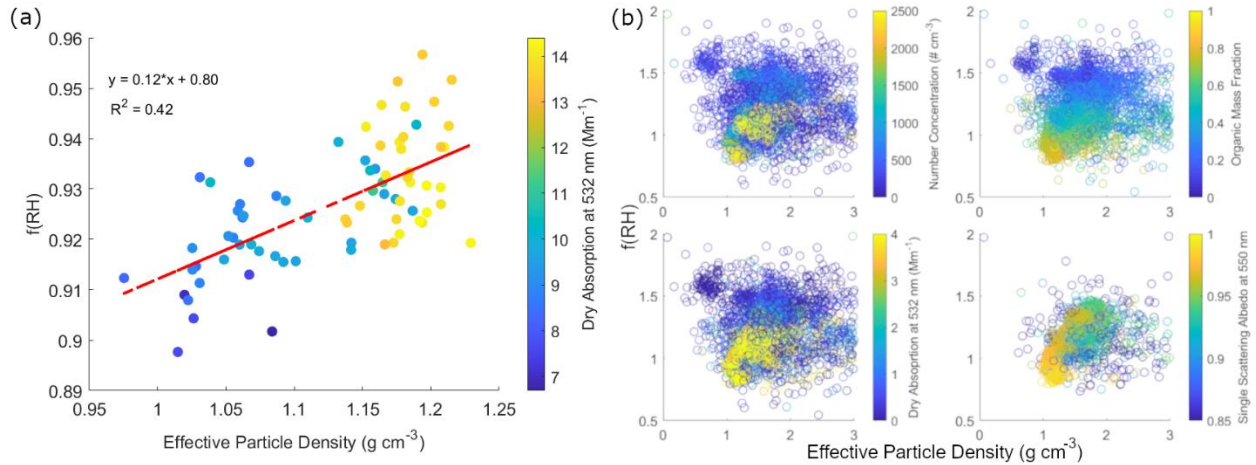
Figure 8. **Effective particle density and *f*(RH).** **30 s *f*(RH=82 % ± 10 %/RH<40 %) at 550 nm and effective particle density plots for (a) 16 September 2019 from 01:00 to 01:40 UTC colored by dry absorption at 532 nm and with (red) linear regression line and (upper left) corresponding equation and goodness of fit, and (b) for the entire CAMP²Ex field campaign and colored by (clockwise from top left) LAS number concentration of particles with diameters between 100 and 1000 nm, organic mass fraction, single scattering albedo at 550 nm, and dry absorption at 532 nm.**

524   Smoke particles are known to have a range of density values, depending on their degree of atmospheric aging, affecting

525   their size, and the processes they undergo. The effective particle density is usually lower for biomass burning particles

526   from smoldering that have larger diameters (Pokhrel et al., 2021), compared to flaming. Freshly emitted smoldering

527   particles have effective densities from 1.03 g cm⁻³ to 1.21 g cm⁻³ that do not vary much with diameter based on a

528   laboratory study (Pokhrel et al., 2021). Our calculated values fall within this range (Fig. 8). This adds confidence to

529   our observation that organics (brown carbon), which dominate smoldering emissions, are the major contributors to the

530   sub-1 *f*(RH). Both aerosol hygroscopicity and effective particle density are important for properly modeling cloud

531   condensation nuclei, one of the most important factors in aerosol-cloud interactions.

532   **3.2.2 Vertical Transport**

533   The vertical distribution of aerosols affects cloud formation, we investigate this through two cases of aerosol vertical

534   transport. The vertical transport cases were identified from averages of the available vertical profiles made during

535   CAMP²Ex. A large-scale event (01:53 to 06:20 UTC 20 Sep 2019) north of Luzon, Philippines, due to a tropical

536   cyclone, and a smaller-scale event (02:55 to 06:02 UTC 24 Sep 2019) east of Luzon, due to shallow convection were

537   chosen for the case studies. The measured median CO mixing ratio was used as a tracer for vertical transport (Kar et

538   al., 2004). An increase in the median CO mixing ratio at higher altitudes along with multi-level winds from a similar

539   direction were the main criteria used to identify the cases.

540   Northerly to northwesterly winds are the dominant source for the first case (Fig. 9a) influenced by tropical cyclone

541   Tapah (TC Tapah's center was ~600 km northeast of the aircraft location). This suggests the influence of East Asia

542   on the sample as described in Crosbie et al. (2022), where the meteorology is discussed in more detail. There is a

543   general decrease in *f*(RH) from the lower levels that follows a similar trend to the decrease in total mass (Fig. 9b) and

544 sulfate mass fraction. Sulfate is hygroscopic so it is understandable that the f(RH) decreased with altitude as the sulfate

545 mass fraction decreased. The increase in CO between 6-7 km (Fig. 9b) suggests vertical transport aloft and was

546 accompanied by a subsequent decrease in f(RH) and ammonium mass fraction and increase in organic mass fraction

547 (Fig. 9b) between 6-8 km. This is consistent with analysis in previous sections, which show decreased f(RH) with

548 increased organic mass fractions.

549 Accompanying the general decrease of f(RH) with altitude are decreasing submicrometer median volume size

550 distribution (VSD) magnitudes and volume weighted average diameters (Fig. 10). Possible reasons for these trends

551 are that larger hygroscopic particles, such as sulfate (which make up the largest mass fraction at lower levels), were

552 scavenged (especially at lower altitudes) and/or activated into cloud drops, leaving the smaller particles behind.

553 Submicrometer aerosol mass also decreases with altitude, with values below 1 µg m^{-3} (Fig. 9b). There is a slight

554 increase in VSD magnitude from 6-8 km compared to 4-6 km, and especially at larger diameters, broadening the VSD

555 curve which may suggest cloud processing (Eck et al., 2012). Though sulfate enhancements have traditionally been

556 the marker for cloud processes (Barth et al., 2000; Faloona, 2009), more recent studies have observed potential cloud

557 processing cases with increased organics (i.e. Wonaschuetz et al., 2012; Dadashazar et al., 2022). This case could

558 thus be showing vertically transported organic matter that has possibly affected or was affected by the clouds between

559 6-7 km. Another observation is the increase of ammonium and nitrate mass fractions above 4 km (Fig. 9b). There is

560 no corresponding valid f(RH) data, and we can only infer based on the CO profile that begins to shift toward a more

561 positive slope with increasing altitude that this increase in ammonium could also be associated with cloud processing.

562 Ammonia is abundant in East Asia (Pawar et al., 2021) and although there are still limited studies, the scavenging

563 efficiencies of organics and ammonium (compared to sulfate) could also be contributing to their increasing mass

564 fractions with altitude (Yang et al., 2015; Hilario et al., 2025).

565
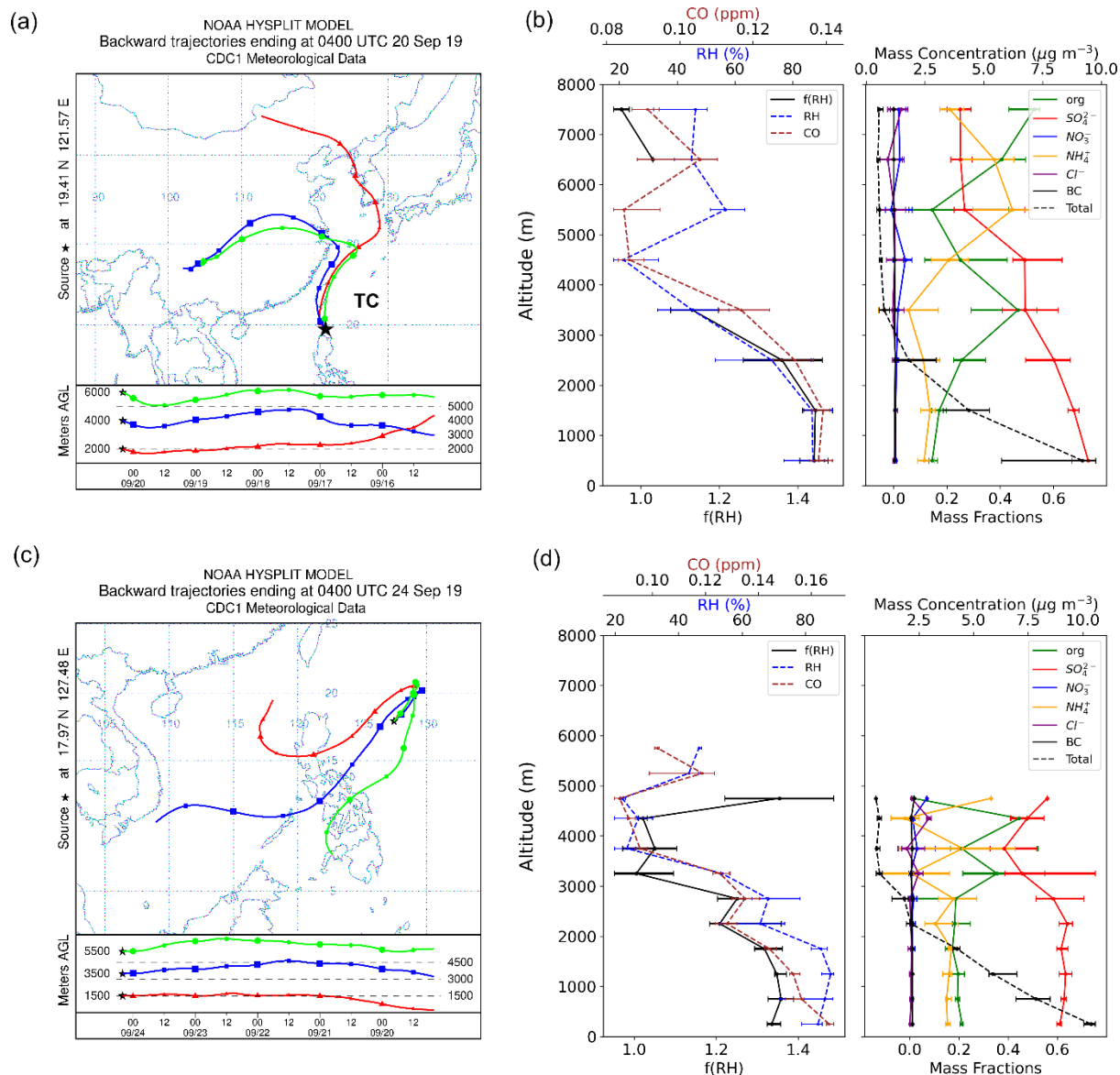
Figure 9. **Case studies of (a-b) tropical cyclone-induced convection on 20 September 2019 and (c-d) shallow convection on 24 September 2019. (a) Five-day multi-level back trajectories from the average location of the aircraft from 01:53 to 06:20 UTC with the approximate TC center location and (b) vertical profiles (median, 25 and 75th percentiles) of (left) f(RH=82 % ± 10 %/RH<40 %) at 550 nm, relative humidity (RH), and CO mixing ratio and (right) submicrometer mass fractions of organics, sulfate, nitrate, ammonium, and black carbon and sum of mass concentrations from AMS and SP2 (dashed black line) for 1 km altitude bins, (c) five-day multi-level back trajectories from the average location of the aircraft from 02:55 to 06:02 UTC, and (d) vertical profiles of f(RH=82 % ± 10 %/RH<40 %) at 550 nm, relative humidity (RH), CO mixing ratio, and submicrometer mass fractions and sum of mass concentrations from AMS and SP2 for 0.5 km altitude bins.**
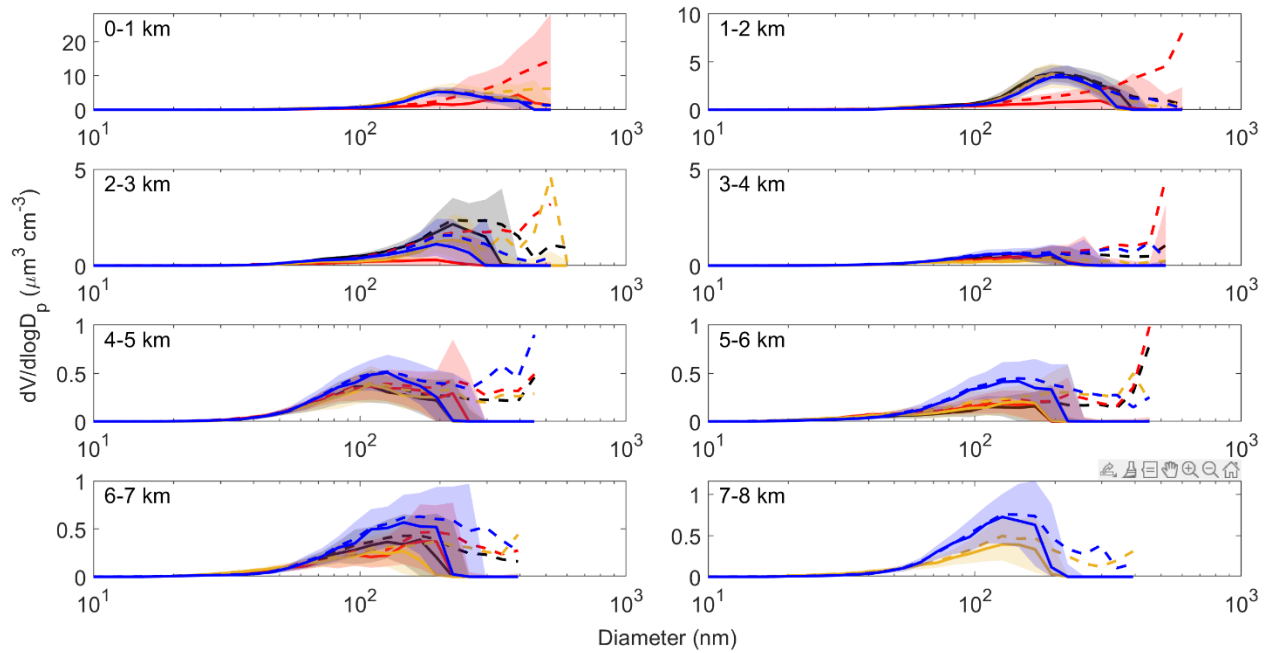
Figure 10. Volume size distributions for the tropical cyclone-induced convection case study. Median (solid line), mean (dashed line), and 25th to 75th percentiles (shaded area) of volume size distributions of submicrometer particles (FIMS) every 1 km altitude ~~for the case study of tropical cyclone-induced convection~~ on 20 September 2019 from 01:53 to 06:20 UTC. The colors represent four separate vertical profiles, where black was from 01:35 to 02:19 UTC, red was from 03:40 to 04:44 UTC, yellow was from 04:59 to 05:27 UTC, and blue was from 05:52 to 06:20 UTC.

The second case, the shallow cumulus case on 24 September 2019 (Hilario et al., 2025), has multi-level wind trajectories initially from the West Pacific in the northeast direction, which appear to have come from the Philippines and the general southwest direction from two days before (Fig. 9c). The most evident increase in CO (Fig. 9d) is observed between 5-5.5 km, at an altitude lower than the previous case. Both RH and f(RH) have a similar trend to CO throughout the vertical profile, which slightly follows the trend of sulfate mass fraction. This is observed especially in the lower levels (until ~2 km) where RH and f(RH) are relatively steady, even with a large decrease in total aerosol mass.

At higher altitudes, above 4.5 km, f(RH) increases to a greater degree with decreased organic mass fraction and increased sulfate mass fraction (Fig. 9d), possibly due to cloud processing. Like the first case, the VSD plots (Fig. 11) for this case show decreasing VSD magnitudes and volume weighted average diameters with increasing altitudes. The broadening of the VSDs above 3 km, concurrent with the ~~increased~~ decreased sulfate mass fraction, likewise suggests cloud processing. There is a known sulfate source, a power plant in western Luzon, in the Philippines that is along the path of the l.5 km back trajectory (Fig. 9c) and may possibly contribute to sulfate in the region (Lorenzo et al., 2023). It is possible that this and other sulfate sources in the region, such as those from ships (Miller et al., 2023), are being transported vertically and affecting aerosol hygroscopicity in the areas where there is shallow convection.

596
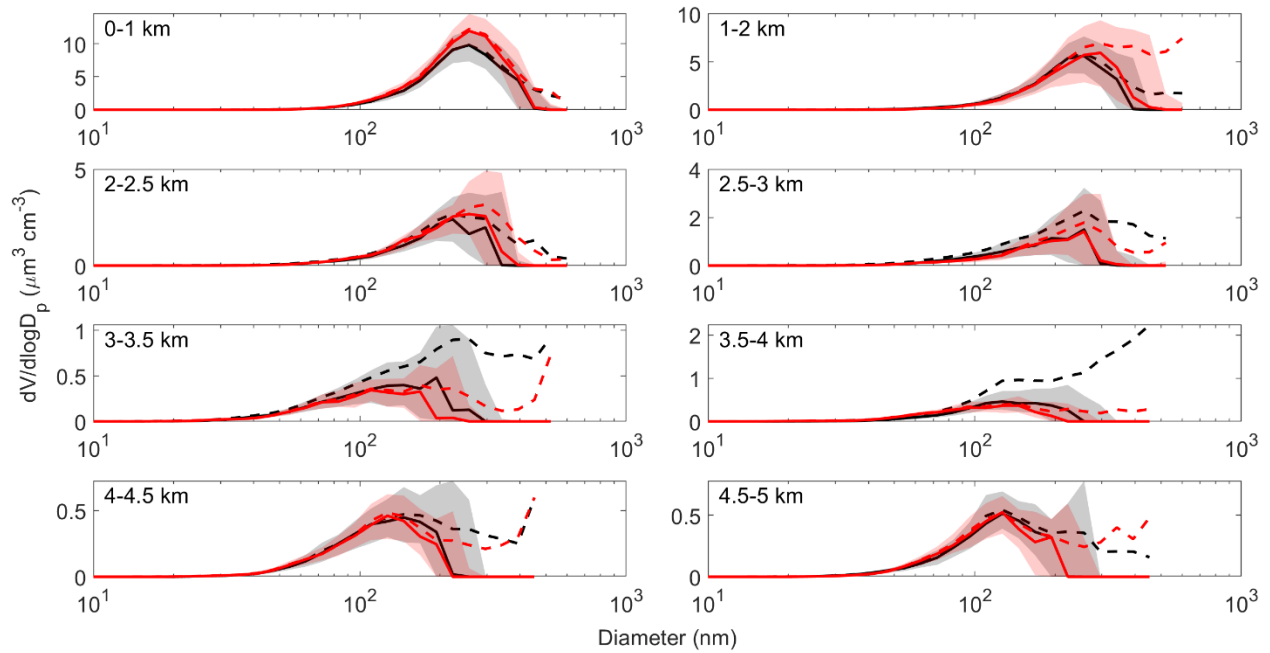
Figure 11. Volume size distributions for the shallow convection case study. Median (solid line), mean (dashed line), and 25th to 75th percentiles (shaded area) of volume size distributions of submicrometer particles (FIMS) in 0.5-1 km altitude increments ~~for the case study of shallow convection~~ on 24 September 2019 from 02:55 to 06:02 UTC. The colors represent two separate vertical profiles, where black was from 02:55 to 04:07 UTC and red was from 05:42 to 06:02 UTC.

601 In summary, for both cases vertical transport in cumulus clouds correspond to higher f(RH) with lower organic mass
602 fractions or increased sulfate mass fractions, at cloud outflow altitudes. At slightly higher altitudes, increasing organics
603 with decreasing ammonium decrease f(RH) for the tropical cyclone case. The VSD magnitudes and the averaged
604 diameter of the aerosol size decrease from cloud base to cloud outflow altitudes, with the VSDs broadening likely due
605 to cloud processing. The understanding and representation of the vertical transport or aerosols due to the tropical
606 cyclone and shallow convection and their role in aerosol-cloud interaction is further investigated as we evaluate
607 modeled data using the two cases that we have just discussed.

608 **3.2.3   Model Evaluation**

609 To give regional context to the cases, we begin the discussion of model evaluation with the horizontal distribution of
610 the modeled (~111 km resolution) near-surface aerosol hygroscopicity (kappa: calculated from the volume fractions
611 and kappa values (Eq. 3) of the modeled submicrometer aerosol species as described in 2.3.2) and winds within the
612 CAMP[2]Ex domain. We will compare the model kappa values to kappa from different regions around the world based
613 on previous studies. Subsequently, we will discuss how the modeled submicrometer kappa at different vertical levels
614 compare to the kappa derived from bulk f(RH) (< 5 µm) (Eqs. 4 and 5) as well as from kappa derived from
615 submicrometer AMS and SP2 species (Eq. 3) from the aircraft observations.

616 The CAM-chem modeled surface kappa values (Fig. 12) in the CAMP[2]Ex region of interest, during the time when the
617 three cases discussed in 3.2.1 and 3.2.2 were sampled, are within the range of globally modeled surface kappa in clean

618 marine (0.9 – 1.0), continental (0.1 – 0.4), and continental outflow / polluted marine (0.4 – 0.6) regions from previous

619 studies (Pringle et al., 2010). The highest modeled kappa (~1.0, Figs. 12a and 12b) is like those previously found in

620 clean marine areas. The high kappa values are influenced by the strong winds, which can increase sea salt emissions,

621 due to the tropical cyclone which was still developing on 16 September 2019 and more fully developed on 20

622 September 2019. The Pacific Ocean also is the source of high kappa (~0.9 - 1.0) for the shallow convection case on

623 24 September 2019 (Fig. 12c). For all three cases there was low kappa (< 0.4) in areas with low wind speeds and over

624 land especially over Borneo and East Asia, typical of continental and continental outflow regions. For the two cases

625 that were within the southwest monsoon (Figs. 13a and 13b) the lowest kappa values (< 0.2) were in Borneo and

626 downwind areas including Southern Philippines and areas east of it.

627 The modeled surface kappa (~0.1 – 0.5) below the aircraft positions for the case studies of interest (pink lines in Fig.

628 12), though over the sea, are lower than in those areas most affected by the Pacific Ocean and are influenced by

629 emissions from Borneo (Figs. 7a and 12a), East Asia (Figs. 9a and 12b) and the Philippines (Fig. 9c and 12c) based

630 on back trajectories. Kappa, calculated from the median f(RH) derived from scattering measurements, for the five air

631 masses discussed in sections 3.1 and 3.2 (MC: -0.02, EA: 0.14, PSEA: 0.10, WP: 0.24, and Other: 0.11), all fall in the

632 continental category even though the majority of these air masses are technically in regions with continental outflow

633 or polluted marine regions. The CAM-chem kappa values for the aircraft positions for the case studies with vertical

634 transport (Figs. 12b and 12c) the CAM-chem kappa values (~0.40 – 0.50) are more than double the range of calculated

635 kappa from East Asia (0.14) and Other (0.11) air masses that are influencing the case studies. To make sense of this

636 difference between globally modeled surface kappa values and that which is calculated from the CAMP^{2}Ex f(RH), we

637 delve more into aerosol vertical transport and its connection to aerosol hygroscopicity and evaluate the vertical profile

638 of the kappa calculated from the CAM-chem model outputs.
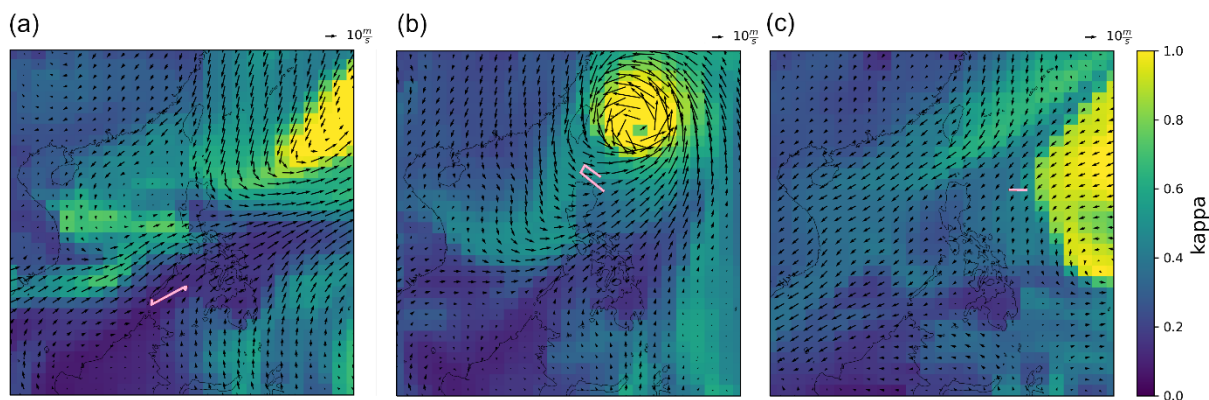
Fig. 12. Modeled kappa and winds at 957 hPa for (a) the biomass burning smoke case at 06:00 UTC on 16 September 2019, (b) the tropical cyclone-induced case at 06:00 UTC on 20 September 2019 and, (c) the shallow convection case at 06:00 UTC on 24 September 2019. The pink lines represent the aircraft locations from 02:15 to 04:22 UTC on 16 September 2019, 01:53 to 06:20 UTC on 20 September 2019 and, from 02:55 to 06:02 UTC on 24 September 2019. The approximate aircraft locations are represented by pink lines.

645   The CAM-chem model (Fig. 13a) was able to represent the general trends in the observed total submicrometer mass

646   vertical profile for the tropical cyclone-induced convection case. The observations from AMS are only for non-

647   refractory aerosol species, however, and so sea salt and dust are not included in the total mass, possibly affecting the

648   comparison with the model output, which accounts for both. The uniform ~111 km grid mesh CAM-chem and

649   MUSICA outputs show approximate contributions by sea salt and dust to be 5 to 20% % of the total mass (Figs. 13d

650   and 13e). This could explain the higher total mass values from the model outputs compared to observations for some

651   altitude levels, though in general even without dust and sea salt the CAM-chem model still has slightly higher aerosol

652   total mass values (dashed lines in Fig. 13a) compared to the observations. The CAM-chem model represents the

653   approximate aerosol total mass well for this case probably because of its large-scale nature, where wind speeds were

654   high (> 20 m s^{-1}) and where the aerosol particles are potentially from a large source (East Asia) (Figs. 9a and 13a).

655   Together, the sum of the sulfate and ammonium mass fractions are similar for the observed (Fig. 13c) and modeled

656   outputs close to the surface (Figs. 13d and 13e), where the model output is ammonium bisulfate and not just sulfate,

657   but the actual mass concentrations of sulfate from the models are generally higher than the observations above 1 km

658   (Fig. S1a). This sulfate-based compound dominates the total aerosol mass for both the observations and model outputs,

659   as is expected based on its source air mass from East Asia, and accounts for the similar observed and modeled total

660   mass shape profiles (Fig. S1). The organic mass fraction, on the other hand, is lower by almost half of the observed

661   organic mass fraction due to sulfate dominating. This has a direct effect on modeled aerosol hygroscopicity (kappa),

662   as it was shown earlier that f(RH) decreases with an increased organic mass fraction (Fig. 4).

663
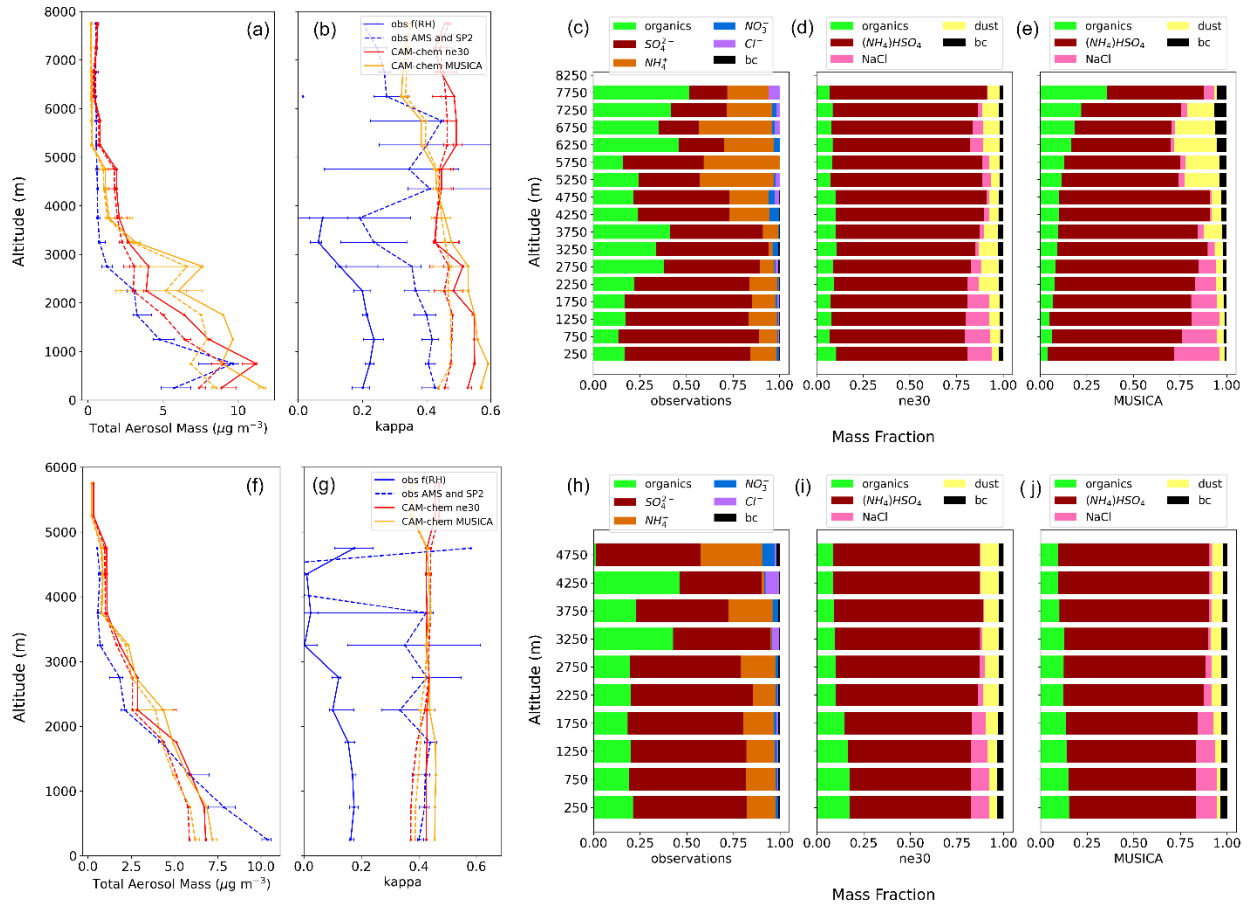
Figure 13. Vertical profiles of observed data and CAM-chem model outputs for ne30 ~1° and MUSICA 0.25° grids for (a-e) the tropical cyclone-induced convection case on 20 September 2019 and (f-j) the shallow convection case on 24 September 2019 at 500 m intervals. (a) Total observed submicrometer aerosol mass (01:53 to 06:20 UTC) from AMS (organics, SO₄²⁻, NO₃⁻, NH₄⁺, Cl⁻) and SP2 (black carbon (BC)) data and CAM-chem output (06:00 UTC) (organics: primary/hydrophobic, hygroscopic, and secondary ($C_{15}H_{38}O_2$), sulfate (NH_4HSO_4), sea salt, dust ($AlSiO_5$), and black carbon (primary/hydrophobic and hygroscopic)) where the solid line includes all the CAM-chem species and the dashed line excludes dust and sea salt and (b) calculated kappa from observed f(RH=82 % ± 10 %/RH<40 %) at 550 nm (solid line, < 5 μm) and from AMS and SP2 (dashed line, submicrometer) data and using ZSR mixing rule for all CAM-chem aerosol species (solid line, submicrometer) and excluding dust and sea salt (dashed line). The lines correspond to the median values of data in the given altitude intervals and the bars correspond to the 25ᵗʰ and 75ᵗʰ percentile values. Submicrometer median mass fractions at 500 m intervals of (c) observational data (01:53 to 06:20 UTC) and (d-e) corresponding CAM-chem model outputs (06:00 UTC) for (d) ne30 ~1° and (e) MUSICA 0.25° grids for the tropical cyclone-induced convection case on 20 September 2019. CAM-chem outputs were combined into five main categories: organics (primary/hydrophobic, hygroscopic, and secondary ($C_{15}H_{38}O_2$)); sulfate (NH_4HSO_4); sea salt; dust ($AlSiO_5$); and black carbon (primary/hydrophobic and hygroscopic). (f) Total observed submicrometer aerosol mass (02:55 to 06:02 UTC) from AMS and SP2 data and (06:00 UTC) CAM-chem output and (g) calculated kappa from observed f(RH=82 % ± 10 %/RH<40 %) and from AMS and SP2 data. Submicrometer median mass fractions of (h) observational data (02:55 to 06:02 UTC) and (i-j) corresponding CAM-chem model outputs (06:00 UTC) for the shallow convection case on 24 September 2019.

Median modeled kappa for the tropical cyclone-induced convection case is more than twice in magnitude compared to the median derived kappa from f(RH) (Fig. 13b), though they have a similar vertical profile shape. It has been noted

686 from previous studies that the conversion of observed f(RH) to kappa (Brock et al., 2016b) may be associated with up
687 to 40% % uncertainty (Van Diedenhoven et al., 2022), though this does not change that the kappa from CAM-chem
688 is still approximately twice the calculated observed kappa. We note that additional uncertainties as a result of the
689 conversion from Brock et al. (2016b) could also be contributing to the discrepancy. Brock et al. (2016b) used
690 submicrometer measurements in the southeast U.S. while CAMP^{2}Ex f(RH) was calculated for particles less than 5
691 µm. Kappa calculated from f(RH) represents larger particles (< 5 µm) compared to the kappa calculated from CAM-
692 chem (< 0.48 µm), and the difference in size of the particles could be contributing to this disparity in kappa.

693 We compare more similar sized particles, kappa derived from AMS and SP2 measurements (< 0.70 µm) with kappa
694 calculated from CAM-chem (Fig. 13b), and find that the kappa derived from the AMS and SP2 is still lower than that
695 computed from CAM-chem outputs. The kappa from AMS and SP2 is approximately twice (100% % larger than) the
696 kappa from f(RH), probably due to more than just particle size differences. Based on Mie theory and studies comparing
697 f(RH) of PM$_1$ and PM$_{10}$ particles (Zieger et al., 2013; Titos et al., 2021), CAMP^{2}Ex f(RH) would be larger if it were
698 measuring just submicrometer particles due to the increased scattering efficiency for accumulation mode particles
699 compared to coarse particles. Though, based on Fig. 3 of Titos et al. (2021), the difference in f(RH) in marine sites
700 would only be ~0.1 (given median observed SAE) and that would translate to ~20 to 40% % increase in kappa. Thus,
701 although size plays a role, composition is also contributing to the difference in the calculated kappa values between
702 observations and the model. Examples of past studies in the region with low kappa values suggest that both the size
703 and compositional effect together are important. Lab experiments of tropical peat burning showed that smaller (70
704 nm) primary organic particles (POA) became more oxidized faster compared to larger particles (150 nm) and kappa
705 for oxidized POA (100 nm) was 0.16 (Chen et al., 2022). Ground measurements of aerosol particles (56 nm – 100 nm)
706 in Quezon City in the Philippines, which were dominated by elemental carbon, yielded kappa values less than 0.10
707 (Azadiaghdam et al., 2019).

708 The over and under-represented mass of sulfates and organics, respectively (Fig. 13b), by the model may be causing
709 the higher kappa in the model. Based on the discussion in section 3.1.2 on air masses coming from East Asia (Fig.
710 4c), as is the case for this event, an organic mass fraction that is lower by half can increase the f(RH) (f(RH = (-0.81
711 * organic mass fraction) + 1.56) and therefore the derived kappa by ~70% %. Organics, especially secondary organic
712 aerosols have been underpredicted by CAM-chem in urban and urban outflow regions (Schwantes et al., 2022). This
713 is consistent with the observations for this case, which is influenced by urban outflow from East Asia and thus affecting
714 the calculated kappa from the model. CO (Fig. S1) is also underrepresented by the model potentially due to emissions
715 inventories (Hua et al., 2024).

716 For the case of shallow convection, the shape of the vertical profile of the CAM-chem model output total mass
717 concentration is similar to the observed total mass concentration profile (Fig. 13f), though it underestimates the
718 observed total concentration by approximately 2 to 4.5 µg m^{-3} below 1 km altitude, and then overestimates
719 concentrations by approximately 0.5 to 2 µg m^{-3} above 1 km. This is due to the model underestimating organics and
720 sulfate close to the surface, while sulfate is overestimated above 1 km (Fig. S1b). The effect of this is seen in the

model-derived kappa, which is, like the previous case, higher than the calculated kappa from observations, though to a lesser degree (Fig. 13g). Unlike the case of the tropical cyclone-induced convection, the modeled kappa is relatively unchanging in shape compared to the kappa derived from observations. This is likely due to the differences in the compositional profile at the higher altitudes, even if the total mass is similar. The model is not able to represent the increase and decrease in organic mass fraction from 3.5 to 4.5 km (Fig. 13h) and dominance of sulfate above 4.5 km. At those altitudes the observations become dominated by sulfate, ammonium, and nitrate (Fig. 13h), even with losses due to scavenging and activation as shown by decreased aerosol mass with altitude, probably due to the in-cloud production of sulfate as discussed in section 3.2.2. The mass fraction profiles from the model (Figs. 13i and 13j) appear to have a steadily decreasing (increasing) organic and sea salt (sulfate and dust) mass fraction with height. This case is a smaller scale event with smaller surface winds associated with it (Fig. 12b) compared to the tropical cyclone case. With weak forcing, it is likely that the CAM cumulus parameterizations does not predict the convection observed in the shallow convection case affecting modeled aerosol mass vertical distribution and, consequently, kappa in both the uniform ~1°1 global model and the regionally refined simulations. This is similar to a model evaluation study (i.e. GEOS and GOCART) of CAMP²Ex aerosol extinction data, which recommended an improvement of shallow convection schemes to improve the representation of vertical transport (Collow et al., 2022). In fact, the CO increase above 5 km, that that we used to identify convection, is not captured by CAM-chem (Fig. S2). What is consistent though is that for both the observations and model output of this shallow convection case, the relative magnitude of the model kappa is lower than that of the tropical cyclone case.

4. Conclusion

This study reports on low PM_5 (D_p < 5 µm) aerosol hygroscopicity measured during CAMP²Ex 2019 in Southeast Asia due to organics from biomass burning. Aging and vertical transport changes the hygroscopicity of particles affecting clouds in the region. Comparisons with a global atmospheric chemistry model reveal discrepancies between observed and modeled aerosol concentrations and hygroscopicity, emphasizing the need to improve emissions inventories and shallow cloud parameterizations. Notable results of this work, following the study goals raised at the end of Section 1 are as follows:

The generally low median f(RH) (1.24 with Q1 and Q3 of 1.05 and 1.43, respectively) of aerosol particles (< 5 µm) in Southeast Asia during the CAMP²Ex campaign from 24 August to 5 October in 2019 is linked to the dominating regional effect of biomass burning from the Maritime Continent. Measurements of f(RH) in other polluted marine environments around the world for PM_{10} (< 10 µm) and PM_1 (< 1 µm) particles have higher ranges (median of ~1.7 – 2.0) of f(RH) values (Titos et al., 2021). The median f(RH) of air masses from the Maritime Continent was exceptionally low (1.05 with Q1 and Q3 of 0.94 and 1.20, respectively) for polluted marine environments and are more similar to those with biomass burning (Gomez et al., 2018). The air masses with the highest f(RH) from CAMP²Ex are generally from the West Pacific, in the northernmost regions of the Philippines and farthest away from the Maritime Continent. Their median f(RH) (1.49 with Q1 and Q3 of 1.26 and 1.73, respectively) is also lower than what has been associated with typical polluted marine environments.

Throughout CAMP²Ex, submicrometer organic matter is the main aerosol component associated with biomass burning and the low f(RH) values. Organics are a major feature of total aerosol mass, especially in air masses traced back to the Maritime Continent. Biomass burning smoke is spread out in the region increasing AOD downwind of the MC (Fig. 2 in Reid et al. (2023)) and is corroborated by cases of sub-1 f(RH) and submicrometer reflective particles with elevated organic mass fractions that are present in all the air masses. Based on clustering analysis using optical properties, majority of the particles sampled during the campaign appear to be a mixture of both organic and elemental carbon. Organics dominate in terms of mass fraction due to the smoldering-type burning in peat fire (Reid et al., 2023) from the Maritime Continent, which is known to produce more organics than elemental carbon (Reid et al., 2005). This is consistent with what Miller et al. (2023) observed where the highest median levels of organic and elemental carbon mass during CAMP²Ex were due to biomass burning from the Maritime Continent. Without organics, the baseline f(RH) (1.38 – 1.55, Fig. 4), is still lower than measurements from other areas (i.e. ~1.8 from the Yangtze River Delta in China and from INDOEX over the Indian Ocean, 2.19 from SEAC⁴RS in and around the U.S., ~2.6 from ICARTT over North America and Europe, ~3 from ACE-ASIA over the Yellow Sea and Sea of Japan, and ~3.5 from Melpitz, Germany) (Shingler et al., 2016a) (Zhang et al., 2015; Quinn et al., 2005; Shingler et al., 2016a; Zieger et al., 2014) probably due to the presence of elemental carbon, which is the second most dominant aerosol type during the campaign. The unique relationship between organic matter and hygroscopicity in the CAMP²Ex region is important information that can help in model evaluations (Burgos et al., 2020).

Farther away from the Maritime Continent, the organic particles have aged and become more oxidized as they interacted with the other air masses. The West Pacific is a remote region in northern Philippines and is downwind of biomass burning from MC, resulting in a combined marine and polluted aerosol. The oldest biomass burning aerosols were observed there. The organic oxidation values of the aerosol particles in the air mass from the West Pacific are close to the threshold of maximum oxidation that has been observed in previous studies (Cubison et al., 2011). Vertical transport decreases and increases hygroscopicity at cloud level with increased organic and sulfate mass fractions, respectively, in the West Pacific. These aerosol constituents are thought to be transported from the MC and the Philippines and their surrounding oceans, where natural and industrial sources are significant (Miller et al., 2023), and then cloud processed.

Evaluation of the global chemical transport CAM-chem model at two output grids (~111 km and 25 km) against two convective cases from CAMP²Ex show the underrepresentation of organics in general and a higher derived aerosol hygroscopicity (kappa), which may be linked to the possible overestimation of aerosol hygroscopicity from biomass burning based on studies of aerosol optical depth and extinction in the area (Collow et al., 2022; Edwards et al., 2022). CAM-chem overestimates sulfate in the tropical cyclone induced convection case, consistent with results from an assessment of the NAAPS reanalysis product on the positive bias of sulfate from East Asia (Edwards et al., 2022). The vertical representation of the aerosol composition for the larger scale convection case due to a tropical cyclone is better than that for the shallow convection case. Cloud processing and increased hygroscopicity are not captured by the model for the shallow convection case, irrespective of model grid size. The representation of shallow convection in the area by global models remains challenging, based on other model-evaluation studies (Collow et al., 2022). Past

studies on biomass burning aerosol effects on convection in Southeast Asia using a cloud-scale model emphasized the importance of aerosol composition and absorptive properties, and their effect on atmospheric stability, in the understanding of aerosol-cloud interactions (Hodzic and Duvel, 2018). It is thus ideal that cloud-scale models be evaluated using the dataset from CAMP²Ex, where the invigoration of shallow clouds has been observed (Reid et al., 2023).

The implications of the low aerosol hygroscopicity in the region and its effects on clouds and climate are just beginning to be unraveled. The mixing and aging of organic and elemental carbon from biomass burning smoke in the Maritime Continent with background and transported sources influences hygroscopicity observations and modeling uncertainties and can be the topic of future work. Improvements in harmonization in terms of aerosol particle sizes and composition, along with updated emissions inventories, will be helpful moving forward both for the observations and modeling of aerosol hygroscopicity. These suggestions can hopefully improve shallow cumulus representation, which is still the biggest source of differences in model sensitivity in the understanding of climate change (Bony and Dufresne, 2005), in the region and globally. Emerging endeavors to implement higher resolution schemes in a large domain (Pfister et al., 2020; Radtke et al., 2021) to capture both fine scale aerosol-cloud processes along with improved observations in Southeast Asia hold promise.

Data availability. CAMP²Ex data archived per research flight and parameter type can be found at:
https://doi.org/10.5067/Airborne/CAMP2Ex_Aerosol_AircraftInSitu_P3_Data_1

https://doi.org/10.5067/Suborbital/CAMP2EX2018/DATA001(P-3 In-Situ Aerosol Data),
https://doi.org/10.5067/Airborne/CAMP2Ex_Cloud_AircraftInSitu_P3_Data_1 (P-3 In-Situ Cloud Data),
https://doi.org/10.5067/Airborne/CAMP2Ex_MetNav_AircraftInSitu_P3_Data_1 (P-3 In-Situ Meteorological and Navigational Data), and https://doi.org/10.5067/Airborne/CAMP2Ex_TraceGas_AircraftInSitu_P3_Data_1 (P-3 In-Situ Trace Gas Data). CAM-chem model outputs can be found at https://doi.org/10.6084/m9.figshare.26755936.v1.

Author contributions. LDZ, ECC, JPDG, GSD, RF, MRAH, MS, JW, QX, and AS carried out various aspects of the data collection. ST and JZ conducted the CAM-chem model simulations. GRL, LDZ, AFA, MB, ECC, RF, MRAH, MS, JW, QX, and AS performed analysis and interpretation of the data. GRL and AS prepared the manuscript with contributions from the coauthors.

Competing interests. At least one of the (co-)authors is a member of the editorial board of *Atmospheric Chemistry and Physics.*

Special issue statement. This article is part of the special issue "Cloud Aerosol and Monsoon Processes Philippines Experiment (CAMP²Ex) (ACP/AMT inter-journal SI)". It is not associated with a conference.

Acknowledgements. The authors gratefully acknowledge the NOAA Air Resources Laboratory (ARL) for the provision of the HYSPLIT transport and dispersion model and READY website (https://www.ready.noaa.gov) used in this publication. The NSF National Center for Atmospheric Research is a major facility sponsored by the U.S. National Science Foundation under Cooperative Agreement No. 1852977.

Financial support. This research has been supported by the National Aeronautics and Space Administration (grant no. 80NSSC18K0148) and ONR grant N00014-21-1-2115.

References

Adam, M. G., Tran, P. T., Bolan, N., and Balasubramanian, R.: Biomass burning-derived airborne particulate matter in Southeast Asia: A critical review, Journal of Hazardous Materials, 407, 124760, https://doi.org/10.1016/j.jhazmat.2020.124760, 2021.

Amnuaylojaroen, T.: Air Pollution Modeling in Southeast Asia—An Overview, Vegetation Fires and Pollution in Asia, 531-544, https://doi.org/10.1007/978-3-031-29916-2_31, 2023.

Anderson, T. L. and Ogren, J. A.: Determining aerosol radiative properties using the TSI 3563 integrating nephelometer, Aerosol Science and Technology, 29, 57-69, https://doi.org/10.1080/02786829808965551, 1998.

Ångström, A.: On the atmospheric transmission of sun radiation and on dust in the air, Geografiska Annaler, 11, 156-166, https://doi.org/10.1080/20014422.1929.11880498, 1929.

Attwood, A., Washenfelder, R., Brock, C., Hu, W., Baumann, K., Campuzano-Jost, P., Day, D., Edgerton, E., Murphy, D., and Palm, B.: Trends in sulfate and organic aerosol mass in the Southeast US: Impact on aerosol optical depth and radiative forcing, Geophysical Research Letters, 41, 7701-7709, https://doi.org/10.1002/2014GL061669, 2014.

AzadiAghdam, M., Braun, R. A., Edwards, E.-L., Bañaga, P. A., Cruz, M. T., Betito, G., Cambaliza, M. O., Dadashazar, H., Lorenzo, G. R., and Ma, L.: On the nature of sea salt aerosol at a coastal megacity: Insights from Manila, Philippines in Southeast Asia, Atmos. Environ., 216, 116922, https://doi.org/10.1016/j.atmosenv.2019.116922, 2019.

Barth, M., Rasch, P., Kiehl, J., Benkovitz, C., and Schwartz, S.: Sulfur chemistry in the National Center for Atmospheric Research Community Climate Model: Description, evaluation, features, and sensitivity to aqueous chemistry, J. Geophys. Res.- Atmos., 105, 1387-1415, https://doi.org/10.1029/1999JD900773, 2000.

Baynard, T., Garland, R., Ravishankara, A., Tolbert, M., and Lovejoy, E.: Key factors influencing the relative humidity dependence of aerosol light scattering, Geophysical research letters, 33, https://doi.org/10.1029/2005GL024898, 2006.

Bergstrom, R. W., Pilewskie, P., Russell, P. B., Redemann, J., Bond, T. C., Quinn, P. K., and Sierau, B.: Spectral absorption properties of atmospheric aerosols, Atmos. Chem. Phys., 7, 5937-5943, https://doi.org/10.5194/acp-7-5937-2007, 2007.

Bony, S. and Dufresne, J. L.: Marine boundary layer clouds at the heart of tropical cloud feedback uncertainties in climate models, Geophysical Research Letters, 32, https://doi.org/10.1029/2005GL023851, 2005.

Brock, C., Wagner, N., and Gordon, T.: Effect of Aerosol Size and Hygroscopicity on Aerosol Optical Depth in the Southeastern United States, EGU General Assembly Conference Abstracts,

869 Brock, C. A., Wagner, N. L., Anderson, B. E., Attwood, A. R., Beyersdorf, A., Campuzano-Jost,
870 P., Carlton, A. G., Day, D. A., Diskin, G. S., and Gordon, T. D.: Aerosol optical properties in the
871 southeastern United States in summer-Part 1: Hygroscopic growth, https://doi.org/10.5194/acp-
872 16-4987-2016, 2016b.
873 Brooks, S. D., Wise, M. E., Cushing, M., and Tolbert, M. A.: Deliquescence behavior of
874 organic/ammonium sulfate aerosol, Geophysical Research Letters, 29, 23-21-23-24,
875 https://doi.org/10.1029/2002GL014733, 2002.
876 Burgos, M. A., Andrews, E., Titos, G., Alados-Arboledas, L., Baltensperger, U., Day, D.,
877 Jefferson, A., Kalivitis, N., Mihalopoulos, N., and Sherman, J.: A global view on the effect of
878 water uptake on aerosol particle light scattering, Scientific data, 6, 1-19,
879 https://doi.org/10.1038/s41597-019-0158-7, 2019.
880 Burgos, M. A., Andrews, E., Titos, G., Benedetti, A., Bian, H., Buchard, V., Curci, G., Kipling,
881 Z., Kirkevåg, A., and Kokkola, H.: A global model–measurement evaluation of particle light
882 scattering coefficients at elevated relative humidity, Atmospheric Chemistry and Physics, 20,
883 10231-10258, https://doi.org/10.5194/acp-20-10231-2020, 2020.
884 Cazorla, A., Bahadur, R., Suski, K., Cahill, J. F., Chand, D., Schmid, B., Ramanathan, V., and
885 Prather, K.: Relating aerosol absorption due to soot, organic carbon, and dust to emission sources
886 determined from in-situ chemical measurements, Atmospheric Chemistry and Physics, 13, 9337-
887 9350, https://doi.org/10.5194/acp-13-9337-2013, 2013.
888 Chandra, A. S., Zhang, C., Klein, S. A., and Ma, H. Y.: Low-cloud characteristics over the
889 tropical western Pacific from ARM observations and CAM5 simulations, Journal of Geophysical
890 Research: Atmospheres, 120, 8953-8970, https://doi.org/10.1002/2015JD023369, 2015.
891 Che, H., Segal-Rozenhaimer, M., Zhang, L., Dang, C., Zuidema, P., Dobracki, A., Sedlacek III,
892 A. J., Coe, H., Wu, H., and Taylor, J.: Cloud processing and weeklong ageing affect biomass
893 burning aerosol properties over the south-eastern Atlantic, Communications earth &
894 environment, 3, 182, https://doi.org/10.1038/s43247-022-00517-3, 2022.
895 Chen, J., Budisulistiorini, S. H., Itoh, M., and Kuwata, M.: Roles of relative humidity and
896 particle size on chemical aging of tropical peatland burning particles: Potential influence of
897 phase state and implications for hygroscopic property, Journal of Geophysical Research:
898 Atmospheres, 127, e2022JD036871, https://doi.org/10.1029/2022JD036871, 2022.
899 Chen, J., Zhao, C., Ma, N., and Yan, P.: Aerosol hygroscopicity parameter derived from the light
900 scattering enhancement factor measurements in the North China Plain, Atmospheric Chemistry
901 and Physics, 14, 8105-8118, https://doi.org/10.5194/acp-14-8105-2014, 2014.
902 Chen, Q., McGowan, S., Gouramanis, C., Fong, L., Balasubramanian, R., and Taylor, D.:
903 Rapidly rising transboundary atmospheric pollution from industrial and urban sources in
904 Southeast Asia and its implications for regional sustainable development, Environ. Res. Lett., 15,
905 1040a1045, https://doi.org/10.1088/1748-9326/abb5ce, 2020.
906 Collow, A. B. M., Buchard, V., Colarco, P. R., da Silva, A. M., Govindaraju, R., Nowottnick, E.
907 P., Burton, S., Ferrare, R., Hostetler, C., and Ziemba, L.: An evaluation of biomass burning
908 aerosol mass, extinction, and size distribution in GEOS using observations from CAMP 2 Ex,
909 Atmospheric Chemistry and Physics, 22, 16091-16109, https://doi.org/10.5194/acp-22-16091-
910 2022, 2022.
911 Covert, D. S., Charlson, R., and Ahlquist, N.: A study of the relationship of chemical
912 composition and humidity to light scattering by aerosols, Journal of Applied Meteorology, 11,
913 968-976, https://doi.org/10.1175/1520-0450(1972)011<0968:ASOTRO>2.0.CO;2, 1972.

914 Crosbie, E., Ziemba, L. D., Shook, M. A., Robinson, C. E., Winstead, E. L., Thornhill, K. L.,
915 Braun, R. A., MacDonald, A. B., Stahl, C., and Sorooshian, A.: Measurement report: Closure
916 analysis of aerosol–cloud composition in tropical maritime warm convection, Atmos. Chem.
917 Phys., 22, 13269-13302, https://doi.org/10.5194/acp-22-13269-2022, 2022.
918 Crumeyrolle, S., Gomes, L., Tulet, P., Matsuki, A., Schwarzenboeck, A., and Crahan, K.:
919 Increase of the aerosol hygroscopicity by cloud processing in a mesoscale convective system: a
920 case study from the AMMA campaign, Atmospheric Chemistry and Physics, 8, 6907-6924,
921 https://doi.org/10.5194/acp-8-6907-2008, 2008.
922 Cruz, M. T., Bañaga, P. A., Betito, G., Braun, R. A., Stahl, C., Aghdam, M. A., Cambaliza, M.
923 O., Dadashazar, H., Hilario, M. R., Lorenzo, G. R., Ma, L., MacDonald, A. B., Pabroa, C., Yee,
924 J. R., Simpas, J. B., and Sorooshian, A.: Size-resolved composition and morphology of
925 particulate matter during the southwest monsoon in Metro Manila, Philippines, Atmos. Chem.
926 Phys., 19, 10675–10696, https://doi.org/10.5194/acp-19-10675-2019, 2019.
927 Cubison, M., Ortega, A., Hayes, P., Farmer, D., Day, D., Lechner, M., Brune, W., Apel, E.,
928 Diskin, G., and Fisher, J.: Effects of aging on organic aerosol from open biomass burning smoke
929 in aircraft and laboratory studies, Atmospheric Chemistry and Physics, 11, 12049-12064,
930 https://doi.org/10.5194/acp-11-12049-2011, 2011.
931 Dadashazar, H., Corral, A. F., Crosbie, E., Dmitrovic, S., Kirschler, S., McCauley, K., Moore,
932 R., Robinson, C., Schlosser, J. S., and Shook, M.: Organic enrichment in droplet residual
933 particles relative to out of cloud over the northwestern Atlantic: analysis of airborne ACTIVATE
934 data, Atmos Chem Phys, 22, 13897-13913, 2022.
935 Delene, D. J. and Ogren, J. A.: Variability of aerosol optical properties at four North American
936 surface monitoring sites, Journal of the Atmospheric Sciences, 59, 1135-1150,
937 https://doi.org/10.1175/1520-0469(2002)059<1135:VOAOPA>2.0.CO;2, 2002.
938 Dockery, D. W.: Epidemiologic evidence of cardiovascular effects of particulate air pollution,
939 Environmental health perspectives, 109, 483-486, https://doi.org/10.1289/ehp.01109s4483, 2001.
940 Doherty, S. J., Quinn, P. K., Jefferson, A., Carrico, C. M., Anderson, T. L., and Hegg, D.: A
941 comparison and summary of aerosol optical properties as observed in situ from aircraft, ship, and
942 land during ACE-Asia, Journal of Geophysical Research: Atmospheres, 110,
943 https://doi.org/10.1029/2004JD004964, 2005.
944 Dong, X., Fu, J. S., Huang, K., Lin, N.-H., Wang, S.-H., and Yang, C.-E.: Analysis of the co-
945 existence of long-range transport biomass burning and dust in the subtropical West Pacific
946 Region, Scientific Reports, 8, 8962, https://doi.org/10.1038/s41598-018-27129-2, 2018.
947 Dubovik, O., Holben, B., Eck, T. F., Smirnov, A., Kaufman, Y. J., King, M. D., Tanré, D., and
948 Slutsker, I.: Variability of absorption and optical properties of key aerosol types observed in
949 worldwide locations, J. Atmos. Sci., 59, 590-608, https://doi.org/10.1175/1520-
950 0469(2002)059<0590:VOAAOP>2.0.CO;2, 2002.
951 Dumka, U., Kaskaoutis, D., Sagar, R., Chen, J., Singh, N., and Tiwari, S.: First results from light
952 scattering enhancement factor over central Indian Himalayas during GVAX campaign, Science
953 of the Total Environment, 605, 124-138, https://doi.org/10.1016/j.scitotenv.2017.06.138, 2017.
954 Duplissy, J., DeCarlo, P. F., Dommen, J., Alfarra, M. R., Metzger, A., Barmpadimos, I., Prevot,
955 A. S., Weingartner, E., Tritscher, T., and Gysel, M.: Relating hygroscopicity and composition of
956 organic aerosol particulate matter, Atmospheric Chemistry and Physics, 11, 1155-1165,
957 https://doi.org/10.5194/acp-11-1155-2011, 2011.
958 Eck, T. F., Holben, B. N., Reid, J., Giles, D., Rivas, M., Singh, R. P., Tripathi, S., Bruegge, C.,
959 Platnick, S., and Arnold, G.: Fog-and cloud-induced aerosol modification observed by the

Aerosol Robotic Network (AERONET), J. Geophys. Res.- Atmos., 117, https://doi.org/10.1029/2011JD016839, 2012.

Edwards, E.-L., Reid, J. S., Xian, P., Burton, S. P., Cook, A. L., Crosbie, E. C., Fenn, M. A., Ferrare, R. A., Freeman, S. W., and Hair, J. W.: Assessment of NAAPS-RA performance in Maritime Southeast Asia during CAMP 2 Ex, Atmospheric Chemistry and Physics, 22, 12961-12983, https://doi.org/10.5194/acp-22-12961-2022, 2022.

Eldering, A., Ogren, J., Chowdhury, Z., Hughes, L. S., and Cass, G. R.: Aerosol optical properties during INDOEX based on measured aerosol particle size and composition, Journal of Geophysical Research: Atmospheres, 107, INX2 33-31-INX32 33-38, https://doi.org/10.1029/2001JD001572, 2002.

Engelhart, G., Asa-Awuku, A., Nenes, A., and Pandis, S.: CCN activity and droplet growth kinetics of fresh and aged monoterpene secondary organic aerosol, Atmospheric Chemistry and Physics, 8, 3937-3949, https://doi.org/10.5194/acp-8-3937-2008, 2008.

Faloona, I.: Sulfur processing in the marine atmospheric boundary layer: A review and critical assessment of modeling uncertainties, Atmos. Environ., 43, 2841-2854, https://doi.org/10.1016/j.atmosenv.2009.02.043, 2009.

Fan, X., Liu, J., Zhang, F., Chen, L., Collins, D., Xu, W., Jin, X., Ren, J., Wang, Y., and Wu, H.: Contrasting size-resolved hygroscopicity of fine particles derived by HTDMA and HR-ToF-AMS measurements between summer and winter in Beijing: the impacts of aerosol aging and local emissions, Atmospheric Chemistry and Physics, 20, 915-929, https://doi.org/10.5194/acp-20-915-2020, 2020.

Ferrare, R., Melfi, S., Whiteman, D., Evans, K., Poellot, M., and Kaufman, Y.: Raman lidar measurements of aerosol extinction and backscattering: 2. Derivation of aerosol real refractive index, single-scattering albedo, and humidification factor using Raman lidar and aircraft size distribution measurements, Journal of Geophysical Research: Atmospheres, 103, 19673-19689, https://doi.org/10.1029/98JD01647, 1998.

Ferrare, R., Hair, J., Hostetler, C., Shingler, T., Burton, S. P., Fenn, M., Clayton, M., Scarino, A. J., Harper, D., and Seaman, S.: Airborne HSRL-2 measurements of elevated aerosol depolarization associated with non-spherical sea salt, Frontiers in Remote Sensing, 4, 1143944, https://doi.org/10.3389/frsen.2023.1143944, 2023.

Garland, R. M., Ravishankara, A., Lovejoy, E. R., Tolbert, M. A., and Baynard, T.: Parameterization for the relative humidity dependence of light extinction: Organic-ammonium sulfate aerosol, Journal of Geophysical Research: Atmospheres, 112, https://doi.org/10.1029/2006JD008179, 2007.

Garofalo, L. A., Pothier, M. A., Levin, E. J., Campos, T., Kreidenweis, S. M., and Farmer, D. K.: Emission and evolution of submicron organic aerosol in smoke from wildfires in the western United States, ACS Earth and Space Chemistry, 3, 1237-1247, https://doi.org/10.1021/acsearthspacechem.9b00125, 2019.

Gasparini, R., Collins, D. R., Andrews, E., Sheridan, P. J., Ogren, J. A., and Hudson, J. G.: Coupling aerosol size distributions and size-resolved hygroscopicity to predict humidity-dependent optical properties and cloud condensation nuclei spectra, Journal of Geophysical Research: Atmospheres, 111, https://doi.org/10.1029/2005JD006092, 2006.

Gogoi, M. M., Babu, S. S., Jayachandran, V., Moorthy, K. K., Satheesh, S., Naja, M., and Kotamarthi, V.: Optical properties and CCN activity of aerosols in a high-altitude Himalayan environment: Results from RAWEX-GVAX, Journal of Geophysical Research: Atmospheres, 120, 2453-2469, https://doi.org/10.1002/2014JD022966, 2015.

Gomez, S. L., Carrico, C., Allen, C., Lam, J., Dabli, S., Sullivan, A., Aiken, A. C., Rahn, T., Romonosky, D., and Chylek, P.: Southwestern US biomass burning smoke hygroscopicity: The role of plant phenology, chemical composition, and combustion properties, Journal of Geophysical Research: Atmospheres, 123, 5416-5432, https://doi.org/10.1029/2017JD028162, 2018.

Hänel, G.: The properties of atmospheric aerosol particles as functions of the relative humidity at thermodynamic equilibrium with the surrounding moist air, in: Advances in geophysics, Elsevier, 73-188, https://doi.org/10.1016/S0065-2687(08)60142-9, 1976.

Hegg, D., Larson, T., and Yuen, P. F.: A theoretical study of the effect of relative humidity on light scattering by tropospheric aerosols, Journal of Geophysical Research: Atmospheres, 98, 18435-18439, https://doi.org/10.1029/93JD01928, 1993.

Hilario, M. R. A., Barth, M., Bennett, R., Crosbie, E., DiGangi, J. P., Diskin, G. S., Lorenzo, G. R., Rutledge, S., Martin, M. Y., and Ziemba, L.: Quantifying scavenging efficiencies of different aerosol species and size-resolved volume concentrations in tropical convective clouds over the West Pacific, Journal of the Atmospheric Sciences, 82, 267-282, https://doi.org/10.1175/JAS-D-24-0064.1, 2025.

Hilario, M. R. A., Crosbie, E., Shook, M., Reid, J. S., Cambaliza, M. O. L., Simpas, J. B. B., Ziemba, L., DiGangi, J. P., Diskin, G. S., and Nguyen, P.: Measurement report: Long-range transport patterns into the tropical northwest Pacific during the CAMP 2 Ex aircraft campaign: chemical composition, size distributions, and the impact of convection, Atmos. Chem. Phys., 21, 3777-3802, https://doi.org/10.5194/acp-21-3777-2021, 2021.

Hodzic, A. and Duvel, J. P.: Impact of biomass burning aerosols on the diurnal cycle of convective clouds and precipitation over a tropical island, Journal of Geophysical Research: Atmospheres, 123, 1017-1036, https://doi.org/10.1002/2017JD027521, 2018.

Hong, Y. and Di Girolamo, L.: Cloud phase characteristics over Southeast Asia from A-Train satellite observations, Atmos. Chem. Phys., 20, 8267-8291, https://doi.org/10.5194/acp-20-8267-2020, 2020.

Höpner, F., Bender, F. M., Ekman, A. M., Andersson, A., Gustafsson, Ö., and Leck, C.: Investigation of two optical methods for aerosol-type classification extended to a Northern Indian Ocean site, Journal of Geophysical Research: Atmospheres, 124, 8743-8763, https://doi.org/10.1029/2018JD029685, 2019.

Hua, W., Lou, S., Huang, X., Xue, L., Ding, K., Wang, Z., and Ding, A.: Diagnosing uncertainties in global biomass burning emission inventories and their impact on modeled air pollutants, Atmospheric Chemistry and Physics, 24, 6787-6807, https://doi.org/10.5194/acp-24-6787-2024, 2024.

Kalberer, M.: Aerosol physics and chemistry, Encyclopedia of Atmospheric Sciences, 1, 23, 2014.

Kar, J., Bremer, H., Drummond, J. R., Rochon, Y. J., Jones, D. B., Nichitiu, F., Zou, J., Liu, J., Gille, J. C., and Edwards, D. P.: Evidence of vertical transport of carbon monoxide from Measurements of Pollution in the Troposphere (MOPITT), Geophysical research letters, 31, 2004.

Kavouras, I. G., Nikolich, G., Etyemezian, V., DuBois, D. W., King, J., and Shafer, D.: In situ observations of soil minerals and organic matter in the early phases of prescribed fires, Journal of Geophysical Research: Atmospheres, 117, https://doi.org/10.1029/2011JD017420, 2012.

Köhler, H.: The nucleus in and the growth of hygroscopic droplets, Transactions of the Faraday Society, 32, 1152-1161, 1936.

Kreidenweis, S. and Asa-Awuku, A.: Aerosol Hygroscopicity: Particle water content and its role in atmospheric processes, https://doi.org/10.1016/B978-0-08-095975-7.00418-6, 2014.

Kuang, Y., Zhao, C., Tao, J., Bian, Y., Ma, N., and Zhao, G.: A novel method for deriving the aerosol hygroscopicity parameter based only on measurements from a humidified nephelometer system, Atmospheric Chemistry and Physics, 17, 6651-6662, https://doi.org/10.5194/acp-17-6651-2017, 2017.

Kuang, Y., He, Y., Xu, W., Zhao, P., Cheng, Y., Zhao, G., Tao, J., Ma, N., Su, H., and Zhang, Y.: Distinct diurnal variation in organic aerosol hygroscopicity and its relationship with oxygenated organic aerosol, Atmospheric Chemistry and Physics, 20, 865-880, 2020.

Lacagnina, C., Hasekamp, O. P., Bian, H., Curci, G., Myhre, G., van Noije, T., Schulz, M., Skeie, R. B., Takemura, T., and Zhang, K.: Aerosol single-scattering albedo over the global oceans: Comparing PARASOL retrievals with AERONET, OMI, and AeroCom models estimates, Journal of Geophysical Research: Atmospheres, 120, 9814-9836, https://doi.org/10.1002/2015JD023501, 2015.

Lee, H.-H., Iraqui, O., Gu, Y., Yim, S. H.-L., Chulakadabba, A., Tonks, A. Y.-M., Yang, Z., and Wang, C.: Impacts of air pollutants from fire and non-fire emissions on the regional air quality in Southeast Asia, Atmos. Chem. Phys., 18, 6141-6156, https://doi.org/10.5194/acp-18-6141-2018, 2018.

Li, G., Bei, N., Cao, J., Huang, R., Wu, J., Feng, T., Wang, Y., Liu, S., Zhang, Q., and Tie, X.: A possible pathway for rapid growth of sulfate during haze days in China, Atmos. Chem. Phys., 17, 3301-3316, https://doi.org/10.5194/acp-17-3301-2017, 2017.

Liu, H., Zhao, C., Nekat, B., Ma, N., Wiedensohler, A., Van Pinxteren, D., Spindler, G., Müller, K., and Herrmann, H.: Aerosol hygroscopicity derived from size-segregated chemical composition and its parameterization in the North China Plain, Atmospheric Chemistry and Physics, 14, 2525-2539, https://doi.org/10.5194/acp-14-2525-2014, 2014.

Liu, J. and Li, Z.: Significant underestimation in the optically based estimation of the aerosol first indirect effect induced by the aerosol swelling effect, Geophysical Research Letters, 45, 5690-5699, https://doi.org/10.1029/2018GL077679, 2018.

Liu, X., Ma, P.-L., Wang, H., Tilmes, S., Singh, B., Easter, R., Ghan, S., and Rasch, P.: Description and evaluation of a new four-mode version of the Modal Aerosol Module (MAM4) within version 5.3 of the Community Atmosphere Model, Geoscientific Model Development, 9, 505-522, https://doi.org/10.5194/gmd-9-505-2016, 2016.

Lorenzo, G. R., Arellano, A. F., Cambaliza, M. O., Castro, C., Cruz, M. T., Di Girolamo, L., Gacal, G. F., Hilario, M. R. A., Lagrosas, N., Ong, H. J., Simpas, J. B., Uy, S. N., and Sorooshian, A.: An emerging aerosol climatology via remote sensing over Metro Manila, the Philippines, Atmospheric Chemistry and Physics, 23, 10579-10608, https://doi.org/10.5194/acp-23-10579-2023, 2023.

Malm, W. C. and Day, D. E.: Estimates of aerosol species scattering characteristics as a function of relative humidity, Atmospheric Environment, 35, 2845-2860, https://doi.org/10.1016/S1352-2310(01)00077-2, 2001.

Mason, B., Wagner, N., Adler, G., Andrews, E., Brock, C., Gordon, T., Lack, D., Perring, A., Richardson, M., and Schwarz, J.: An intercomparison of aerosol absorption measurements conducted during the SEAC4RS campaign, Aerosol Science and Technology, 52, 1012-1027, https://doi.org/10.1080/02786826.2018.1500012, 2018.

1096 Maudlin, L., Wang, Z., Jonsson, H., and Sorooshian, A.: Impact of wildfires on size-resolved
1097 aerosol composition at a coastal California site, Atmospheric Environment, 119, 59-68,
1098 https://doi.org/10.1016/j.atmosenv.2015.08.039, 2015.
1099 McNaughton, C. S., Clarke, A. D., Howell, S. G., Pinkerton, M., Anderson, B., Thornhill, L.,
1100 Hudgins, C., Winstead, E., Dibb, J. E., and Scheuer, E.: Results from the DC-8 Inlet
1101 Characterization Experiment (DICE): Airborne versus surface sampling of mineral dust and sea
1102 salt aerosols, Aerosol Science and Technology, 41, 136-159,
1103 https://doi.org/10.1080/02786820601118406, 2007.
1104 Miller, R. M., Rauber, R. M., Di Girolamo, L., Rilloraza, M., Fu, D., McFarquhar, G. M.,
1105 Nesbitt, S. W., Ziemba, L. D., Woods, S., and Thornhill, K. L.: Influence of natural and
1106 anthropogenic aerosols on cloud base droplet size distributions in clouds over the South China
1107 Sea and West Pacific, Atmospheric Chemistry and Physics, 23, 8959-8977,
1108 https://doi.org/10.5194/acp-23-8959-2023, 2023.
1109 Mochida, M., Kuwata, M., Miyakawa, T., Takegawa, N., Kawamura, K., and Kondo, Y.:
1110 Relationship between hygroscopicity and cloud condensation nuclei activity for urban aerosols in
1111 Tokyo, Journal of Geophysical Research: Atmospheres, 111,
1112 https://doi.org/10.1029/2005JD006980, 2006.
1113 Moosmüller, H. and Sorensen, C.: Small and large particle limits of single scattering albedo for
1114 homogeneous, spherical particles, J. Quant. Spectrosc. Ra., 204, 250-255,
1115 https://doi.org/10.1016/j.jqsrt.2017.09.029, 2018.
1116 Nakajima, T., Higurashi, A., Takeuchi, N., and Herman, J. R.: Satellite and ground-based study
1117 of optical properties of 1997 Indonesian forest fire aerosols, Geophysical Research Letters, 26,
1118 2421-2424, https://doi.org/10.1029/1999GL900208, 1999.
1119 NASA, E. D.: Fires in Kalimantan, Indonesia, 2020.
1120 Oanh, N. K., Upadhyay, N., Zhuang, Y.-H., Hao, Z.-P., Murthy, D., Lestari, P., Villarin, J.,
1121 Chengchua, K., Co, H., and Dung, N.: Particulate air pollution in six Asian cities: Spatial and
1122 temporal distributions, and associated sources, Atmospheric environment, 40, 3367-3380,
1123 https://doi.org/10.1016/j.atmosenv.2006.01.050, 2006.
1124 Othman, M., Latif, M. T., Hamid, H. H. A., Uning, R., Khumsaeng, T., Phairuang, W., Daud, Z.,
1125 Idris, J., Sofwan, N. M., and Lung, S.-C. C.: Spatial–temporal variability and health impact of
1126 particulate matter during a 2019–2020 biomass burning event in Southeast Asia, Scientific
1127 Reports, 12, 7630, https://doi.org/10.1038/s41598-022-11409-z, 2022.
1128 Palmer, T. Y.: Large fire winds, gases and smoke, Atmospheric Environment (1967), 15, 2079-
1129 2090, https://doi.org/10.1016/0004-6981(81)90241-9, 1981.
1130 Pawar, P. V., Ghude, S. D., Jena, C., Móring, A., Sutton, M. A., Kulkarni, S., Lal, D. M.,
1131 Surendran, D., Van Damme, M., and Clarisse, L.: Analysis of atmospheric ammonia over South
1132 and East Asia based on the MOZART-4 model and its comparison with satellite and surface
1133 observations, Atmospheric Chemistry and Physics, 21, 6389-6409, https://doi.org/10.5194/acp-
1134 21-6389-2021, 2021.
1135 Petters, M. and Kreidenweis, S.: A single parameter representation of hygroscopic growth and
1136 cloud condensation nucleus activity, Atmospheric Chemistry and Physics, 7, 1961-1971,
1137 https://doi.org/10.5194/acp-7-1961-2007, 2007.
1138 Pfister, G. G., Eastham, S. D., Arellano, A. F., Aumont, B., Barsanti, K. C., Barth, M. C.,
1139 Conley, A., Davis, N. A., Emmons, L. K., and Fast, J. D.: The multi-scale infrastructure for
1140 chemistry and aerosols (MUSICA), Bulletin of the American Meteorological Society, 101,
1141 E1743-E1760, https://doi.org/10.1175/BAMS-D-19-0331.1, 2020.

Pokhrel, R. P., Gordon, J., Fiddler, M. N., and Bililign, S.: Impact of combustion conditions on physical and morphological properties of biomass burning aerosol, Aerosol Science and Technology, 55, 80-91, https://doi.org/10.1080/02786826.2020.1822512, 2021.

Pringle, K., Tost, H., Pozzer, A., Pöschl, U., and Lelieveld, J.: Global distribution of the effective aerosol hygroscopicity parameter for CCN activation, Atmospheric Chemistry and Physics, 10, 5241-5255, https://doi.org/10.5194/acp-10-5241-2010, 2010.

Quinn, P. K., Bates, T., Baynard, T., Clarke, A., Onasch, T., Wang, W., Rood, M., Andrews, E., Allan, J., and Carrico, C.: Impact of particulate organic matter on the relative humidity dependence of light scattering: A simplified parameterization, Geophysical Research Letters, 32, https://doi.org/10.1029/2005GL024322, 2005.

Radtke, J., Mauritsen, T., and Hohenegger, C.: Shallow cumulus cloud feedback in large eddy simulations–bridging the gap to storm-resolving models, Atmospheric Chemistry and Physics, 21, 3275-3288, https://doi.org/10.5194/acp-21-3275-2021, 2021.

Reid, J., Koppmann, R., Eck, T., and Eleuterio, D.: A review of biomass burning emissions part II: intensive physical properties of biomass burning particles, Atmos. Chem. Phys., 5, 799-825, https://doi.org/10.5194/acp-5-799-2005, 2005.

Reid, J., Maring, H., Narisma, G., van den Heever, S., Di Girolamo, L., Ferrare, R., Holz, R., Lawson, P., Mace, G., and Simpas, J.: The coupling between tropical meteorology, aerosol lifecycle, convection, and radiation, during the Cloud, Aerosol and Monsoon Processes Philippines Experiment (CAMP 2 Ex), B. Am. Meteorol. Soc., https://doi.org/10.1175/BAMS-D-21-0285.1, 2023.

Reid, J. S., Hyer, E. J., Johnson, R. S., Holben, B. N., Yokelson, R. J., Zhang, J., Campbell, J. R., Christopher, S. A., Di Girolamo, L., and Giglio, L.: Observing and understanding the Southeast Asian aerosol system by remote sensing: An initial review and analysis for the Seven Southeast Asian Studies (7SEAS) program, Atmos. Res., 122, 403-468, https://doi.org/10.1016/j.atmosres.2012.06.005, 2013.

Robinson, M. S., Chavez, J., Velazquez, S., and Jayanty, R.: Chemical speciation of PM2. 5 collected during prescribed fires of the Coconino National Forest near Flagstaff, Arizona, Journal of the Air & Waste Management Association, 54, 1112-1123, https://doi.org/10.1080/10473289.2004.10470985, 2004.

Rolph, G., Stein, A., and Stunder, B.: Real-time environmental applications and display system: READY, Environ. Modell. Softw., 95, 210-228, https://doi.org/10.1016/j.envsoft.2017.06.025, 2017.

Ross, A. D., Holz, R. E., Quinn, G., Reid, J. S., Xian, P., Turk, F. J., and Posselt, D. J.: Exploring the first aerosol indirect effect over Southeast Asia using a 10-year collocated MODIS, CALIOP, and model dataset, Atmospheric Chemistry and Physics, 18, 12747-12764, https://doi.org/10.5194/acp-18-12747-2018, 2018.

Saxena, P., Hildemann, L. M., McMurry, P. H., and Seinfeld, J. H.: Organics alter hygroscopic behavior of atmospheric particles, Journal of Geophysical Research: Atmospheres, 100, 18755-18770, https://doi.org/10.1029/95JD01835, 1995.

Schlosser, J. S., Braun, R. A., Bradley, T., Dadashazar, H., MacDonald, A. B., Aldhaif, A. A., Aghdam, M. A., Mardi, A. H., Xian, P., and Sorooshian, A.: Analysis of aerosol composition data for western United States wildfires between 2005 and 2015: Dust emissions, chloride depletion, and most enhanced aerosol constituents, J. Geophys. Res.- Atmos., 122, 8951-8966, https://doi.org/10.1002/2017JD026547, 2017.

Schuster, G. L., Dubovik, O., and Holben, B. N.: Angstrom exponent and bimodal aerosol size distributions, J. Geophys. Res.- Atmos., 111, https://doi.org/10.1029/2005JD006328, 2006.

Schwantes, R. H., Lacey, F. G., Tilmes, S., Emmons, L. K., Lauritzen, P. H., Walters, S., Callaghan, P., Zarzycki, C. M., Barth, M. C., and Jo, D. S.: Evaluating the impact of chemical complexity and horizontal resolution on tropospheric ozone over the conterminous US with a global variable resolution chemistry model, Journal of Advances in Modeling Earth Systems, 14, e2021MS002889, https://doi.org/10.1029/2021MS002889, 2022.

Shi, J., Hong, J., Ma, N., Luo, Q., He, Y., Xu, H., Tan, H., Wang, Q., Tao, J., and Zhou, Y.: Measurement report: On the difference in aerosol hygroscopicity between high and low relative humidity conditions in the North China Plain, Atmospheric Chemistry and Physics, 22, 4599-4613, https://doi.org/10.5194/acp-22-4599-2022, 2022.

Shingler, T., Crosbie, E., Ortega, A., Shiraiwa, M., Zuend, A., Beyersdorf, A., Ziemba, L., Anderson, B., Thornhill, L., and Perring, A. E.: Airborne characterization of subsaturated aerosol hygroscopicity and dry refractive index from the surface to 6.5 km during the SEAC4RS campaign, Journal of Geophysical Research: Atmospheres, 121, 4188-4210, https://doi.org/10.1002/2015JD024498, 2016a.

Shingler, T., Sorooshian, A., Ortega, A., Crosbie, E., Wonaschütz, A., Perring, A. E., Beyersdorf, A., Ziemba, L., Jimenez, J. L., and Campuzano-Jost, P.: Ambient observations of hygroscopic growth factor and f (RH) below 1: Case studies from surface and airborne measurements, Journal of Geophysical Research: Atmospheres, 121, 13,661-613,677, https://doi.org/10.1002/2016JD025471, 2016b.

Smith, S. J., Aardenne, J. v., Klimont, Z., Andres, R. J., Volke, A., and Delgado Arias, S.: Anthropogenic sulfur dioxide emissions: 1850–2005, Atmos. Chem. Phys., 11, 1101-1116, https://doi.org/10.5194/acp-11-1101-2011, 2011.

Sorooshian, A., Shingler, T., Crosbie, E., Barth, M., Homeyer, C., Campuzano-Jost, P., Day, D., Jimenez, J., Thornhill, K., and Ziemba, L.: Contrasting aerosol refractive index and hygroscopicity in the inflow and outflow of deep convective storms: Analysis of airborne data from DC3, Journal of Geophysical Research: Atmospheres, 122, 4565-4577, https://doi.org/10.1002/2017JD026638, 2017.

Spill, G., Stier, P., Field, P. R., and Dagan, G.: Effects of aerosol in simulations of realistic shallow cumulus cloud fields in a large domain, Atmospheric Chemistry and Physics, 19, 13507-13517, https://doi.org/10.5194/acp-19-13507-2019, 2019.

Stein, A., Draxler, R. R., Rolph, G. D., Stunder, B. J., Cohen, M., and Ngan, F.: NOAA's HYSPLIT atmospheric transport and dispersion modeling system, B. Am. Meteorol. Soc., 96, 2059-2077, https://doi.org/10.1175/BAMS-D-14-00110.1, 2015.

Stockwell, C. E., Jayarathne, T., Cochrane, M. A., Ryan, K. C., Putra, E. I., Saharjo, B. H., Nurhayati, A. D., Albar, I., Blake, D. R., and Simpson, I. J.: Field measurements of trace gases and aerosols emitted by peat fires in Central Kalimantan, Indonesia, during the 2015 El Niño, Atmospheric Chemistry and Physics, 16, 11711-11732, https://doi.org/10.5194/acp-16-11711-2016, 2016.

Stokes, R. and Robinson, R.: Interactions in aqueous nonelectrolyte solutions. I. Solute-solvent equilibria, The Journal of Physical Chemistry, 70, 2126-2131, 1966.

Swietlicki, E., Hansson, H.-C., Hämeri, K., Svenningsson, B., Massling, A., McFiggans, G., McMurry, P. H., Petäjä, T., Tunved, P., and Gysel, M.: Hygroscopic properties of submicrometer atmospheric aerosol particles measured with H-TDMA instruments in various environments—a

1232 review, Tellus B: Chemical and Physical Meteorology, 60, 432-469,
1233 https://doi.org/10.1111/j.1600-0889.2008.00350.x, 2008.
1234 Thalman, R., de Sá, S. S., Palm, B. B., Barbosa, H. M., Pöhlker, M. L., Alexander, M. L., Brito,
1235 J., Carbone, S., Castillo, P., and Day, D. A.: CCN activity and organic hygroscopicity of aerosols
1236 downwind of an urban region in central Amazonia: seasonal and diel variations and impact of
1237 anthropogenic emissions, Atmospheric Chemistry and Physics, 17, 11779-11801,
1238 https://doi.org/10.5194/acp-17-11779-2017, 2017.
1239 Tilmes, S., Mills, M. J., Zhu, Y., Bardeen, C. G., Vitt, F., Yu, P., Fillmore, D., Liu, X., Toon, B.,
1240 and Deshler, T.: Description and performance of a sectional aerosol microphysical model in the
1241 Community Earth System Model (CESM2), Geoscientific Model Development, 16, 6087-6125,
1242 https://doi.org/10.5194/gmd-16-6087-2023, 2023.
1243 Titos, G., Burgos, M. A., Zieger, P., Alados-Arboledas, L., Baltensperger, U., Jefferson, A.,
1244 Sherman, J., Weingartner, E., Henzing, B., and Luoma, K.: A global study of hygroscopicity-
1245 driven light-scattering enhancement in the context of other in situ aerosol optical properties,
1246 Atmospheric Chemistry and Physics, 21, 13031-13050, https://doi.org/10.5194/acp-21-13031-
1247 2021, 2021.
1248 Tsay, S.-C., Hsu, N. C., Lau, W. K.-M., Li, C., Gabriel, P. M., Ji, Q., Holben, B. N., Welton, E.
1249 J., Nguyen, A. X., and Janjai, S.: From BASE-ASIA toward 7-SEAS: A satellite-surface
1250 perspective of boreal spring biomass-burning aerosols and clouds in Southeast Asia,
1251 Atmospheric environment, 78, 20-34, https://doi.org/10.1016/j.atmosenv.2012.12.013, 2013.
1252 van Diedenhoven, B., Hasekamp, O. P., Cairns, B., Schuster, G. L., Stamnes, S., Shook, M., and
1253 Ziemba, L.: Remote sensing of aerosol water fraction, dry size distribution and soluble fraction
1254 using multi-angle, multi-spectral polarimetry, Atmospheric Measurement Techniques, 15, 7411-
1255 7434, https://doi.org/10.5194/amt-15-7411-2022, 2022.
1256 Virkkula, A.: Correction of the calibration of the 3-wavelength Particle Soot Absorption
1257 Photometer (3λ PSAP), Aerosol Science and Technology, 44, 706-712,
1258 https://doi.org/10.1080/02786826.2010.482110, 2010.
1259 Waggoner, A., Weiss, R., and Larson, T.: In-situ, rapid response measurement of H2SO4/(NH4)
1260 2SO4 aerosols in urban Houston: A comparison with rural Virginia, Atmospheric Environment
1261 (1967), 17, 1723-1731, https://doi.org/10.1016/0004-6981(83)90179-8, 1983.
1262 Wang, X., Ye, X., Chen, H., Chen, J., Yang, X., and Gross, D. S.: Online hygroscopicity and
1263 chemical measurement of urban aerosol in Shanghai, China, Atmospheric Environment, 95, 318-
1264 326, https://doi.org/10.1016/j.atmosenv.2014.06.051, 2014.
1265 Wang, Y., Li, Z., Zhang, Y., Du, W., Zhang, F., Tan, H., Xu, H., Fan, T., Jin, X., and Fan, X.:
1266 Characterization of aerosol hygroscopicity, mixing state, and CCN activity at a suburban site in
1267 the central North China Plain, Atmospheric Chemistry and Physics, 18, 11739-11752,
1268 https://doi.org/10.5194/acp-18-11739-2018, 2018.
1269 Wu, Z., Zheng, J., Shang, D., Du, Z., Wu, Y., Zeng, L., Wiedensohler, A., and Hu, M.: Particle
1270 hygroscopicity and its link to chemical composition in the urban atmosphere of Beijing, China,
1271 during summertime, Atmospheric Chemistry and Physics, 16, 1123-1138,
1272 https://doi.org/10.5194/acp-16-1123-2016, 2016.
1273 Xu, W., Ovadnevaite, J., Fossum, K. N., Lin, C., Huang, R.-J., O'Dowd, C., and Ceburnis, D.:
1274 Aerosol hygroscopicity and its link to chemical composition in the coastal atmosphere of Mace
1275 Head: marine and continental air masses, Atmospheric Chemistry and Physics, 20, 3777-3791,
1276 https://doi.org/10.5194/acp-20-3777-2020, 2020.

1277   Yang, Q., Easter, R. C., Campuzano-Jost, P., Jimenez, J. L., Fast, J. D., Ghan, S. J., Wang, H.,
1278   Berg, L. K., Barth, M. C., and Liu, Y.: Aerosol transport and wet scavenging in deep convective
1279   clouds: A case study and model evaluation using a multiple passive tracer analysis approach,
1280   Journal of Geophysical Research: Atmospheres, 120, 8448-8468,
1281   https://doi.org/10.1002/2015JD023647, 2015.
1282   Zhang, F., Wang, Y., Peng, J., Ren, J., Collins, D., Zhang, R., Sun, Y., Yang, X., and Li, Z.:
1283   Uncertainty in predicting CCN activity of aged and primary aerosols, Journal of Geophysical
1284   Research: Atmospheres, 122, 11,723-711,736, https://doi.org/10.1002/2017JD027058, 2017.
1285   Zhang, L., Sun, J., Shen, X., Zhang, Y., Che, H., Ma, Q., Zhang, Y., Zhang, X., and Ogren, J.:
1286   Observations of relative humidity effects on aerosol light scattering in the Yangtze River Delta
1287   of China, Atmospheric Chemistry and Physics, 15, 8439-8454, https://doi.org/10.5194/acp-15-
1288   8439-2015, 2015.
1289   Zhao, G., Zhao, C., Kuang, Y., Bian, Y., Tao, J., Shen, C., and Yu, Y.: Calculating the aerosol
1290   asymmetry factor based on measurements from the humidified nephelometer system, Atmos.
1291   Chem. Phys., 18, 9049-9060, https://doi.org/10.5194/acp-18-9049-2018, 2018.
1292   Zieger, P., Fierz-Schmidhauser, R., Weingartner, E., and Baltensperger, U.: Effects of relative
1293   humidity on aerosol light scattering: results from different European sites, Atmospheric
1294   Chemistry and Physics, 13, 10609-10631, https://doi.org/10.5194/acp-13-10609-2013, 2013.
1295   Zieger, P., Fierz-Schmidhauser, R., Gysel, M., Ström, J., Henne, S., Yttri, K. E., Baltensperger,
1296   U., and Weingartner, E.: Effects of relative humidity on aerosol light scattering in the Arctic,
1297   Atmospheric Chemistry and Physics, 10, 3875-3890, https://doi.org/10.5194/acp-10-3875-2010,
1298   2010.
1299   Zieger, P., Fierz-Schmidhauser, R., Poulain, L., Müller, T., Birmili, W., Spindler, G.,
1300   Wiedensohler, A., Baltensperger, U., and Weingartner, E.: Influence of water uptake on the
1301   aerosol particle light scattering coefficients of the Central European aerosol, Tellus B: Chemical
1302   and Physical Meteorology, 66, 22716, https://doi.org/10.3402/tellusb.v66.22716, 2014.
1303   Ziemba, L. D., Lee Thornhill, K., Ferrare, R., Barrick, J., Beyersdorf, A. J., Chen, G.,
1304   Crumeyrolle, S. N., Hair, J., Hostetler, C., and Hudgins, C.: Airborne observations of aerosol
1305   extinction by in situ and remote-sensing techniques: Evaluation of particle hygroscopicity,
1306   Geophysical Research Letters, 40, 417-422, https://doi.org/10.1029/2012GL054428, 2013.

1307